Draft version June 21, 2019
Typeset using LaTeX **manuscript** style in AASTeX61

# THE MULTIWAVELENGTH POLARIMETRY IN THE FILAMENTARY CLOUD IC5146: II. MAGNETIC FIELD STRUCTURES

Jia-Wei Wang,[1] Shih-Ping Lai,[1] Dan P. Clemens,[2] Chakali Eswaraiah,[3] Wen Ping Chen,[4] and Anil K. Pandey[5]

[1] *Institute of Astronomy and Department of Physics, National Tsing Hua University, Hsinchu 30013, Taiwan*
[2] *Institute for Astrophysical Research, Boston University, 725 Commonwealth Avenue, Boston, MA 02215, USA*
[3] *CAS Key Laboratory of FAST, National Astronomical Observatories, Chinese Academy of Sciences, People's Republic of China*
[4] *Institute of Astronomy, National Central University, Chung-Li 32054, Taiwan*
[5] *Aryabhatta Research Institute of Observational-Sciences (ARIES), India*

## ABSTRACT

The IC5146 cloud is a nearby star forming region in Cygnus, consisting of filaments in a variety of evolutionary stages. We used the optical and near-infrared polarization data toward the IC5146 cloud reported in the first paper of this series to reveal the magnetic fields in this cloud. With the newly released *Gaia* data, we found that the IC5146 cloud may contain two layers: the first layer, associated with the Cocoon Nebula, is at a distance of ∼800 pc, and the second layer, including the densest main filament, is at a distance of ∼600 pc. The averaged H band polarization map revealed a well-ordered magnetic field morphology, with the polarization segments perpendicular to the main filament but parallel to the nearby sub-filaments, consistent with models assuming that magnetic field is regulating cloud evolution. We estimated the magnetic field strength using the Davis-Chandrasekhar-Fermi method, and found that the magnetic field strength is scale with the volume density by a power-law index of $\sim 0.4$ in a density range from $N_{H_2} \sim 10$ cm$^{-3}$ to $3 \times 10^3$ cm$^{-3}$, which is consistent with the ambipolar diffusion model. In addition, the mass-to-flux ratio of

jwwang@gapp.nthu.edu.tw; slai@phys.nthu.edu.tw

the cloud gradually changes from subcritical to supercritical from the cloud envelope to the dense filament ridge. These features are consistent with the strong magnetic field star formation model and suggest that the magnetic field is important in regulating the evolution of the IC5146 cloud.

*Keywords:* ISM: clouds — ISM: magnetic fields — ISM: structure — ISM: individual objects (IC5146) — Polarization

## 1. INTRODUCTION

Observations in the past few decades revealed that dense cores predominately appear in clusters and form from magnetized and turbulent molecular clouds. These molecular clouds are often elongated or filamentary over parsec scales, and the structures are believed to directly influence the star formation process. However, how prestellar cores form in these clouds remain poorly understood. Theoretical studies suggest that both turbulence and magnetic fields inside the clouds may control the star formation and cloud evolution, but their relative importance is still in debate (as reviewed in McKee & Ostriker 2007). Some numerical simulations suggest that increasing the magnetic field strength would decrease the predicted, overly high, star formation rate to values close to the observed rate (Nakamura & Li 2008; Price & Bate 2008). In addition, the magnetic field can also guide the collapsing of clouds (e.g. Nakamura & Li 2008; Van Loo et al. 2014) and stabilize the filamentary structures (e.g. Inutsuka et al. 2015; Seifried & Walch 2015). In contrast, simulations assuming weak magnetic fields find that compression and fragmentation from supersonic turbulence can reproduce core mass functions, consistent with the observed stellar initial mass functions (Padaon & Nordlund 2002; Mac Low & Klessen 2004). Due to the difficulty of measuring the magnetic field structures of molecular clouds, from large to small scales, past observations have been insufficient to settle this debate.

The *Herschel* Gould Belt Survey (André et al. 2010) showed that filamentary structures are ubiquitous in both quiescent and active star-forming regions, where the spatial distribution of gravitationally unstable filaments is consistent with prestellar cores (André et al. 2010; Molinari et al. 2010). In addition, the observed filamentary structures seem to share a universal characteristic width of $\sim 0.1$ pc, regardless of their central column density or environment. These results favor a scenario in which the filaments are first generated in molecular clouds, due to large-scale magneto-hydrodynamic (MHD) turbulence, and fragment into prestellar cores due to gravitational instability (Men'shchikov et al. 2010; Miville-Deschênes et al. 2010; Ward-Thompson et al. 2010).

In contrast, optical and infrared polarization observations toward reddened background starlight show that the orientations of magnetic field are mostly perpendicular to the long axis of main filaments (the parsec-scale overall filamentary structure) (e.g. Franco et al. 2010; Li et al. 2013). Recent *Planck* survey data (Planck Collaboration et al. 2016) further show that most filaments are well aligned with the magnetic field, either being parallel in diffuse interstellar medium or perpendicular in molecular clouds. These results favor strong magnetic field models that the turbulence compression and global gravitational contraction in cloud is regulated by the magnetic field (Nakamura & Li 2008). In addition, observations reveal that almost all filaments have fine sub-filamentary structures extended from the main structure, also known as striations, and these sub-filaments are mostly parallel to the magnetic fields (e.g. Sugitani et al. 2011; Pillai et al. 2010). Molecular line observations show velocity gradients along striations, implying that the magnetic field is likely channelling accretion gas flows toward the main filament (e.g. Palmeirim et al. 2013; Shimajiri et al. 2018).

In addition to the magnetic field morphology, measurements of magnetic field strength are essential to evaluate the relative importance between gravity, magnetic fields, and turbulence. Crutcher et al. (2010) summarized the Zeeman measurements, the most direct method to measure the magnetic field strength, toward 137 HI and molecular clouds, and found that the measured magnetic field strengths were scaled with volume density by a power index of 0.65. This index indicates that contraction of these clouds is isotropic, and hence magnetic fields are likely too weak to confine cloud contraction. The mass-to-flux ratio ($\Lambda$), the relative strength of the gravitational potential compared to the magnetic field flux, estimated from these Zeeman measurements are supercritical in many clouds, which also favors the weak magnetic field model.

The IC5146 cloud is a nearby star-forming region in Cygnus, composed of an HII region named the Cocoon Nebula and an extending dark cloud. The *Herschel* data reveals that the dark cloud consists of a long major filamentary structure and several sub-filament structures extended from or within the main filament, and most of the filaments seem to have a width of $\sim 0.1$ pc (Arzoumanian et al. 2011). The morphology favors that these filaments may originate from converging flows due to large scale MHD turbulence (Arzoumanian et al. 2011, 2013), and it is critical to investigate the role of magnetic fields in the cloud that is considered as forming in strong turbulence condition.

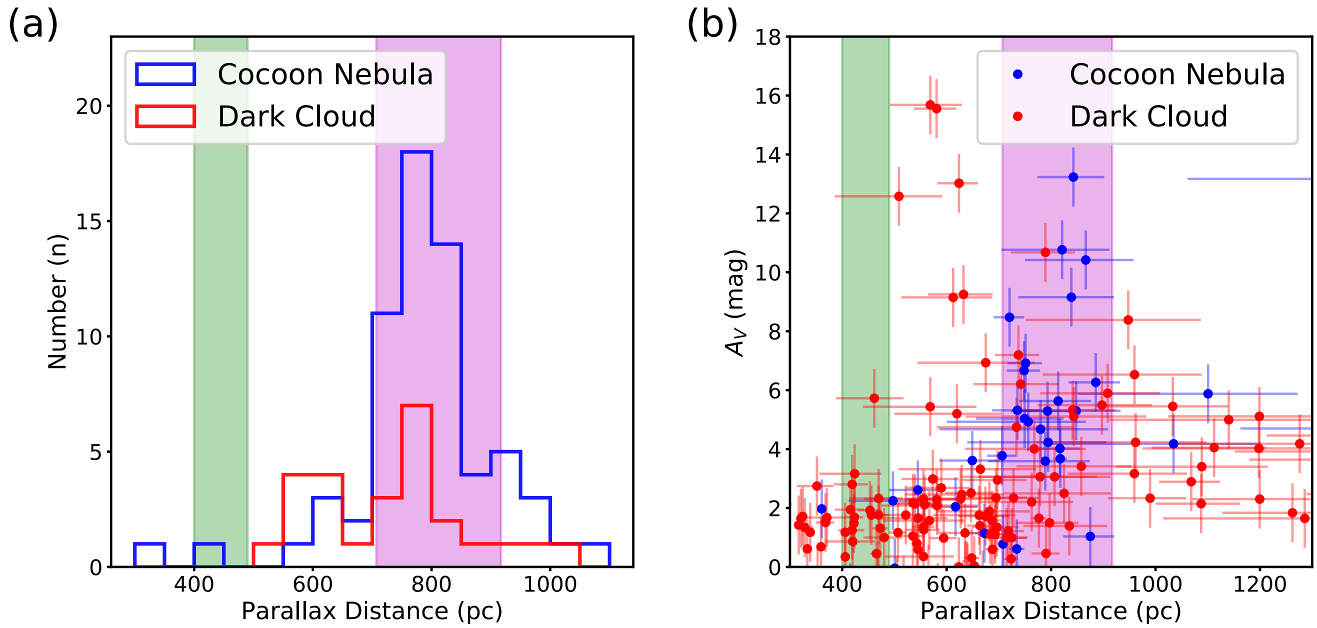


**Figure 1.** (a) Histogram of trigonometric parallax distances to the YSOc in the Cocoon Nebula (blue) and in the dark cloud (red). The YSOc were identified in Harvey et al. (2008) using *Spitzer* data. The parallax distances were measured by Gaia DR2, and we discard those YSOs whose trigonometric parallax is less than $5\sigma$. The green and magenta region labels the distance of $460^{+40}_{-60}$ pc and $813 \pm 106$ pc. The distances of YSOc in the Cocoon Nebula is well consistent with $813 \pm 106$ pc; however, the distances of YSOc in the dark cloud show two peaks appears at distance of $\sim$600 and $\sim$800 pc, suggesting that the dark clouds may be composed by multiple clouds at different distances. The estimation of $460^{+40}_{-60}$ pc might only indicate the distance of the nearest cloud. (b) Visual extinction versus parallax distance of stars within IC5146 dense regions. The stars were selected in the regions where column density was higher than $3 \times 10^{21}$cm$^{-2}$. In the Cocoon Nebula, the $A_V$ of stars arise at a distance of $\sim$700 pc, consistent with the distance estimation of $813 \pm 106$; however, many stars in the dark clouds with $A_V > 3$ mag locates at distance of 500–700 pc, suggest that at least part of the dark cloud is at a shorter distance. The distance estimation of $460^{+40}_{-60}$ pc likely only traces the nearest layer.

Previously published distance estimation for the IC5146 cloud have shown inconsistent results. Harvey et al. (2008) derived a distance of 950 pc based on the comparison of absolute magnitude between the B-type stars within the Cocoon Nebula and to those within the Orion Nebula Cluster. They argued that the IC5146 cloud and the Cocoon Nebula are codistant, because their morphology and velocity distribution seem to be connected. However, Lada et al. (1999) estimated a distance of $460^{+40}_{-60}$ pc via comparing the number of the low extinction foreground stars to those predicted from galactic models. In Paper I, we selected the stars with both polarization and parallax distance measurements near the IC5146 cloud sky area, and showed that polarization percentage rise significantly at a distance of $\sim 400$ pc, which favors the distance estimation of $460^{+40}_{-60}$ pc. The recent *Gaia* data release 2 (DR2) data (Gaia Collaboration et al. 2016, 2018) provides the best parallax measurements up to date, and Dzib et al. (2018) estimated a distance of $813 \pm 106$ pc based on the parallax measurements toward the embedded young stellar objects (YSOs) within the Cocoon Nebula. The origin of these inconsistent distance estimation is still unclear, probably because the dark cloud and the Cocoon Nebula are not codistant, or some of the estimations are incorrect..

In Wang et al. (2017) (hereafter Paper I), we reported our measurements of the starlight polarization over this cloud at both optical and near-infrared wavelengths. The analysis of polarization efficiency suggests that the measured polarization is consistent with dust dichoric polarization and can trace the plane-of-sky magnetic field around IC5146 for $A_V$ up to at least 20 mag. In this paper, we aim at exploring magnetic field properties in the parsec scale based on our starlight polarization measurements, and investigate how the magnetic field correlates with the filamentary structure. In Section 2.1, we reexamine the distance of the Cocoon Nebula and the associated dark clouds using the new *Gaia* data. In Section 2.2, we show the averaged large scale magnetic field morphology based on the polarization measurements toward the IC5146 cloud. Section 2.3 presents the estimation of magnetic field strength. Section 2.4 reports the results of a Bayesian analysis on how magnetic field strength scales with the density. In Section 3, we discuss the results of the analyses and their implication, and in Section 4 present our conclusions. In the forthcoming Paper III, we will present our molecular line observations toward IC5146 to investigate whether the magnetic fields is sufficient to regulate the gas kinematics.

## 2. ANALYSIS

### 2.1. *The Distance of the IC5146 system*

The key issue that causes the ambiguity of the distance estimation of the IC5146 system is whether the Cocoon Nebula and the dark clouds are codistant. The distance estimation using the stars or YSOs within the Cocoon Nebula showed a higher distance of 800–1000 pc (e.g. Harvey et al. 2008; Dzib et al. 2018) while the distance estimation toward the dark clouds favor a distance of 400–500 pc (e.g. Lada et al. 1999; Wang et al. 2017). Hence, we are in a position to believe that either (1) the Cocoon Nebula and the dark clouds are codistant, but one of the distance estimation is incorrect or (2) the Cocoon Nebula and the dark clouds are not codistant (Harvey et al. 2008).

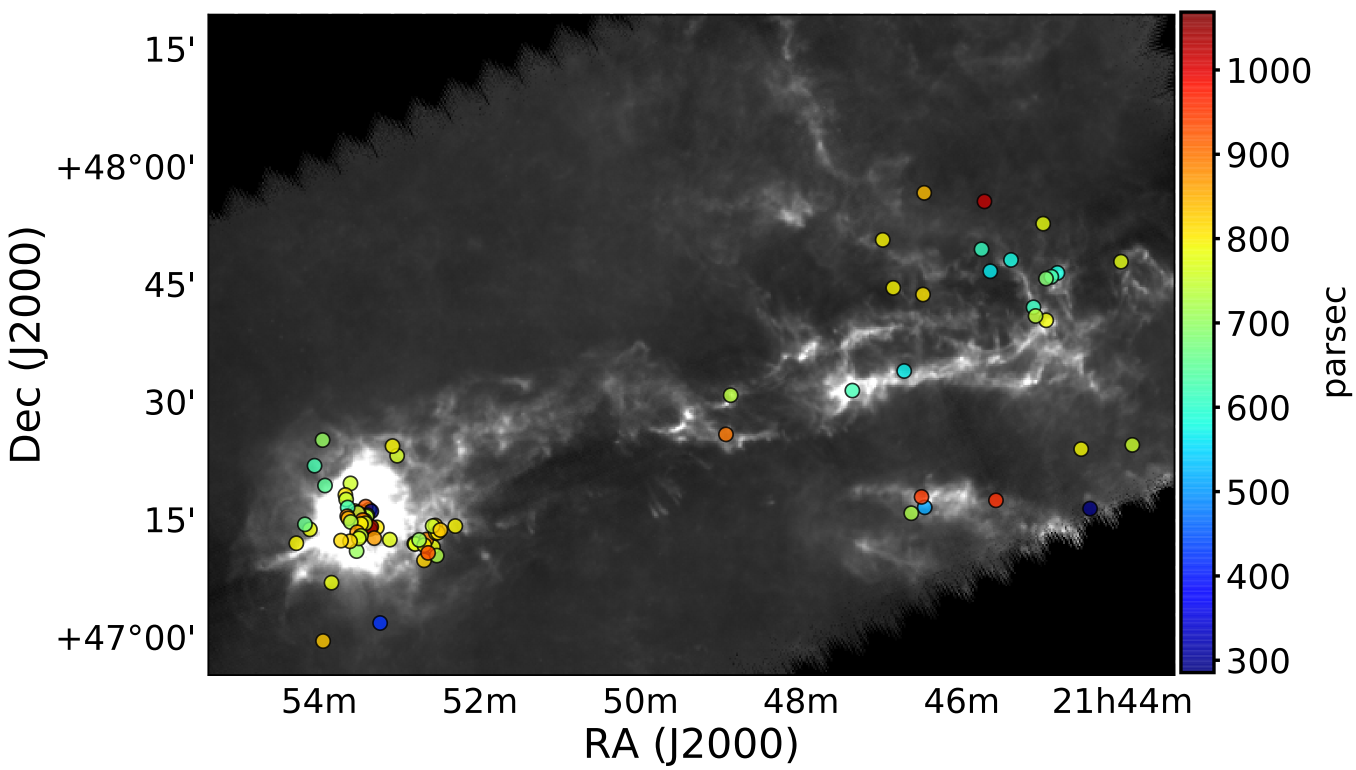


**Figure 2.** The YSOc with distance measurements in the IC5146 cloud system. The YSOc were identified in Harvey et al. (2008) and the color of each point represents its parallax distance estimated from the Gaia DR2 catalog. Most of the YSOc within the Cocoon Nebula have distances of $\sim 800$ pc, but the distances of the YSOc in the dark clouds are widely distributed from 500 to 900 pc. The massive western main filament likely has a distance of $\sim 600$ pc, and thus probably not physically associated with the Cocoon Nebula.

To settle the debate, we used the *Gaia* DR2 data to perform a distance estimation toward both the Cocoon Nebula and the dark clouds. We selected the YSO candidates (YSOc) within the IC5146 system from Harvey et al. (2008), and matched the corresponding parallax measurements in the *Gaia* catalog. We only used those YSOc with $> 5\sigma$ parallax measurements. We excluded the 5 YSOc that have distance measurements greater than 1100 pc, out of the total 98 YSOc, because their distances of 1.1 to 2.6 kpc are much higher than other YSOc, and thus are more likely misidentified background sources. We further separated these YSOc to two groups based on their spatial distribution, in the Cocoon Nebula (R.A. $> 21^h50^m$) and in the dark clouds (R.A. $< 21^h50^m$).

Figure 1 (a) shows the parallax distance measurements toward the YSOc in the Cocoon Nebula and in the dark clouds. The YSOc in the Cocoon Nebula have distances ranging from 600 to 1100 pc and show one major peak at a distance of ∼800 pc, consistent with the previous results (Harvey et al. 2008; Dzib et al. 2018). In contrast, the YSOc in the dark cloud likely show two components, one with a peak at a distance of ∼800 pc similar to the Cocoon Nebula, and the other with a peak a distance of ∼600 pc.

In order to illustrate the distribution of these YSOc, we label the YSOc with the estimated distance overlaid on the *Herschel* 250 $\mu$m map in Figure 2. It clearly shows that most of the stars around the center of the Cocoon Nebula have similar distance of $\sim$ 800 pc. However, the YSOc around the dark clouds have a wide range of distances; the YSOc within the densest filament have similar distances of $\sim$ 600 pc, and the YSOc in the relative diffuse area seem to have distances of $\sim$ 800 pc. We note that because we have relative small number of YSOc distributed over the dark clouds, parts of the dark clouds still lack distance information.

In order to show the distance distribution of the clouds with more samples, we selected the stars, instead of only YSOc, from the *Gaia* DR2 catalog within the regions where the column density, estimated using the *Herschel*, was higher than $3 \times 10^{21}$ cm$^{-2}$, and these stars were matched to our extinction estimation in Paper I. Figure 1 (b) shows the $A_V$ vs parallax distance. Since the uncertainty of our extinction estimation is $\sim$ 1 mag, the stars with $A_V < 2$ mag are possibly the foreground stars. In the Cocoon Nebula, the $A_V > 2$ mag stars is consistent with a distance of ∼800 pc. In the dark clouds, several $A_V > 10$ mag stars appears at distance $> 500$ pc, which is corresponding to the densest filament in the dark cloud and favors a distance of $\sim 600$ pc, although this analysis does not rule out the possibility that part of the dark clouds may be more distant.

Our results suggest that the IC5146 cloud likely consists of two layers. The first layer is at a distance of $\sim 800$ pc, and is associated with the Cocoon Nebula. The second layer is at a distance of $\sim 600$ pc, and contains at least the densest $A_V > 10$ mag main filaments. This could explain why Lada et al. (1999) obtained a distance estimation of 400–500 pc, because the foreground stars they used was located within the $A_V > 10$ mag filament, and therefore traced a lower-limit on the distance of the first layer, which is $\sim 500$ pc. Nevertheless, we do not have sufficient information to show which layer the rest of the filaments are belong to. Hence, in this paper, we adopt a distance of $700 \pm 200$ pc to represent the uncertain distance.

### 2.2. *Magnetic Field Morphology*

In Paper I, we measured the optical and near-infrared starlight polarization over the IC5146 filamentary cloud as shown in Figure 3. The spatial distribution of starlight polarization detection is not uniform and highly depending on the cloud extinction, background star density, and observational condition. The uneven sampling may bias the statistics on the polarization pattern due to the heavier weighting on regions where we have more detection. In order to minimize the uneven sampling effect, we generated the spatially averaged H band polarization map with $3 \times 3$ arcmin bins, which reveals the magnetic field structure at 0.6 pc scale.

The averaged polarization was calculated using all the H band polarization data in Paper I, including the data with low S/N, and only the data with polarization degree less than 0.3% were removed, which is the upper limit of foreground polarization. We calculated the inverse-variance weighted mean Stokes Q and U of the background stars over the $3 \times 3$ arcmin grids, and obtained the mean debiased polarization degree and position angle (PA). Only the polarization values of pixels where the polarization were greater than 3 times their propagated uncertainties are shown in the map.

The spatially averaged polarization map is shown in Figure 4. The map indicates an overall organized 0.6 pc scale magnetic field that appears to have small angular dispersion. In general, the magnetic field is perpendicular to the main filament, and parallel to the sub-filament extending to

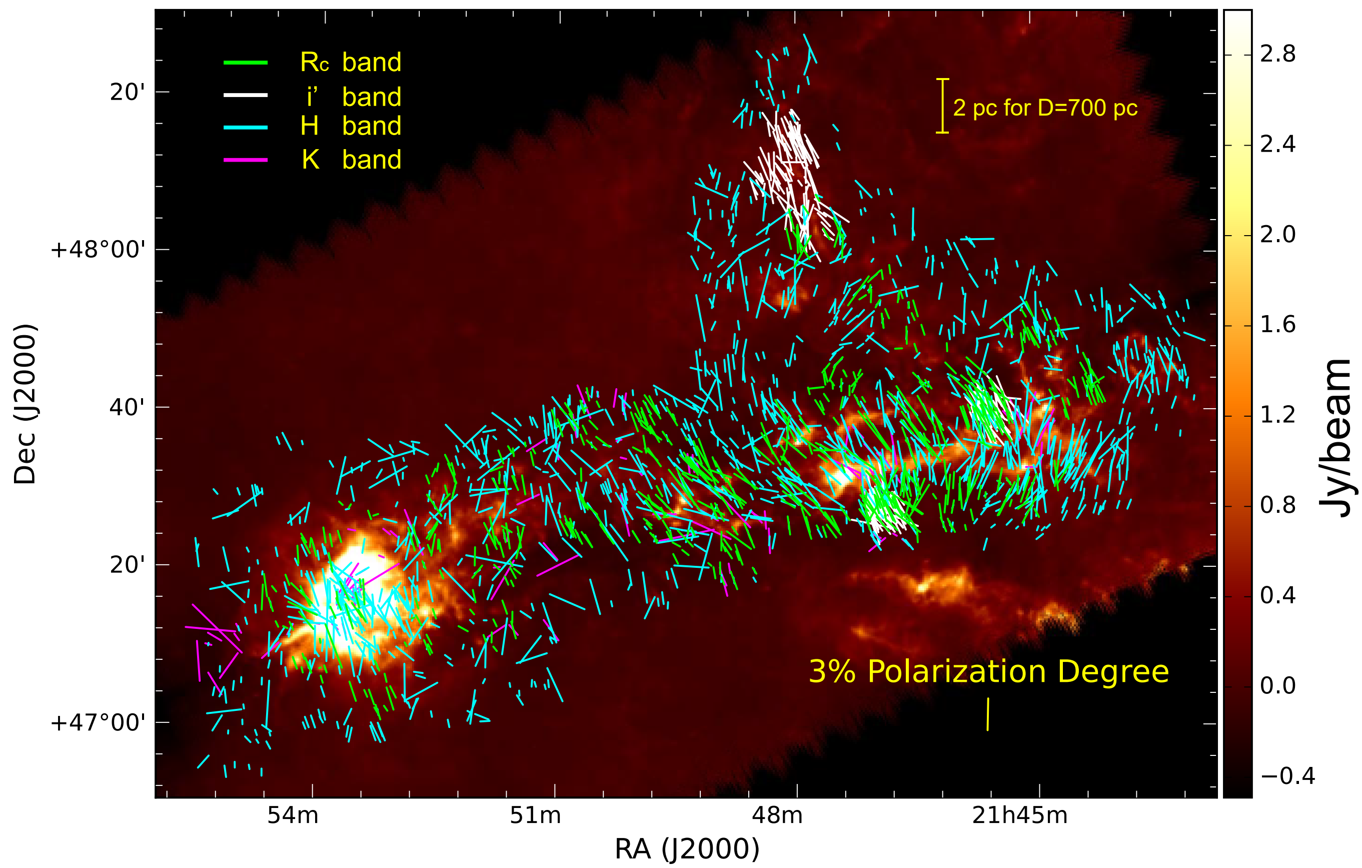


**Figure 3.** Map of IC5146 stellar polarization overlaid on the *Herschel* 250 $\mu$m image. The detection in TRIPOL $i'$-band, AIMPOL $R_c$-band, Mimir $H$- and $K$-band are labeled with white, green, cyan, and magenta.

the north. The magnetic fields in the western part of the cloud likely show a large scale curvature, where the polarization PA changes from -20°to 20°over ∼4 pc.

The IC5146 cloud consists of filaments in a variety of evolutionary stage, and therefore we separated the system into four sub-regions as shown in Figure 5, including (1) the well-known HII region Cocoon Nebula, (2) the eastern part of main filament that is thermally subcritical and lacks of star formation, (3) the western part of main filament that is thermally supercritical and an active star forming region, and (4) the northern filament extended from the main filament structure.

To reveal the overall magnetic field morphology, we show the PA histograms of the smoothed H band data toward the four sub-regions in Figure 6. The four sub-regions all have similar mean PA from 0.°2 to 14.°8. The PA dispersion in the Cocoon Nebula and the eastern main filament are both

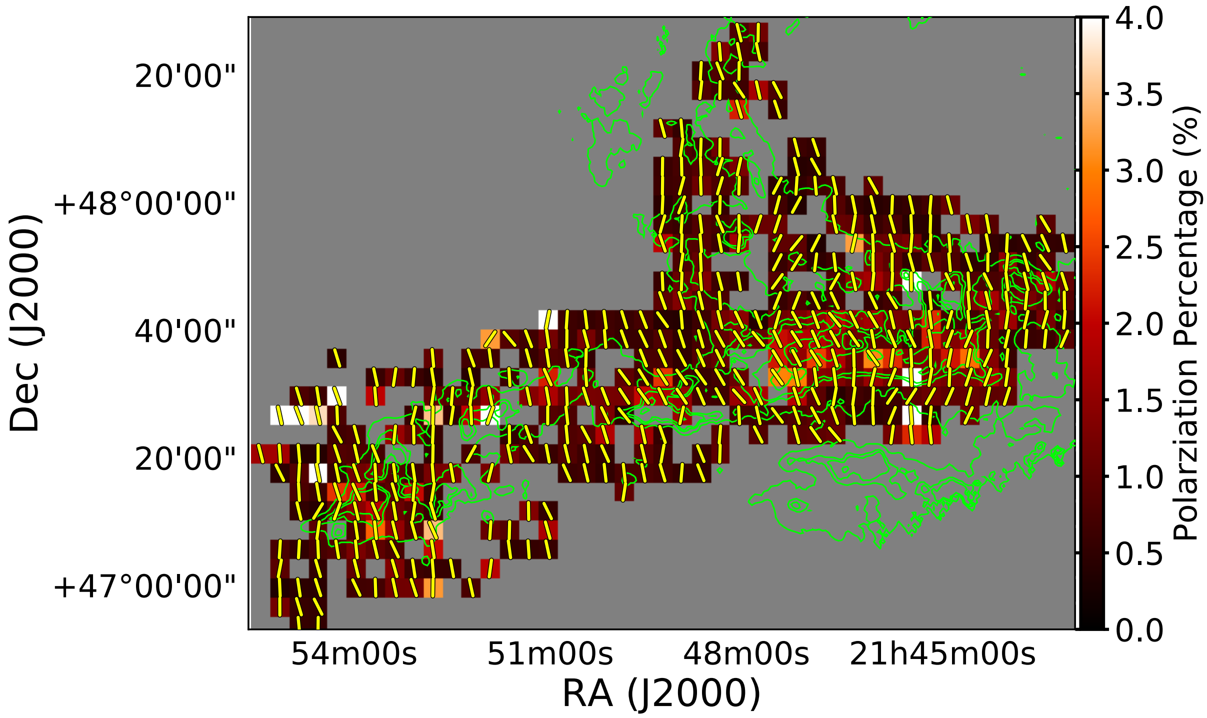


**Figure 4.** Map of spatially averaged H band stellar polarization detection over the IC5146 cloud using $3 \times 3$ arcmin pixels. The pixels show the polarization percentage, the yellow segments represent the orientation of the polarization, and the green contours are the $H_2$ column density with levels of 1, 2, 3, and $10\times(10^{21})$ $cm^{-2}$ calculated by Arzoumanian et al. (2011) using *Herschel* data. The average polarization was only shown if its S/N is greater than 3.

$\sim 12°$, while the western main filament and the northern filament both have higher PA dispersion of $\sim 18°$. We further plot the filament orientation, identified by eyes as plotted in Figure 5, and the histograms show that the magnetic fields is almost perpendicular to the eastern and western main filament, but parallel to the northern filament.

In order to investigate whether the higher PA dispersion in the western main filament is caused by the large scale structure, we plot the PA vs. the radial distance toward the filament in Figure 7. The zero point of the radial distance is set to the blue lines shown in Figure 5, and orientations of the filaments are also labeled. In the eastern main filament, the PA shows no correlation with the radial distance and is always perpendicular to the filament orientation (20°) within 10°. In contrast, the

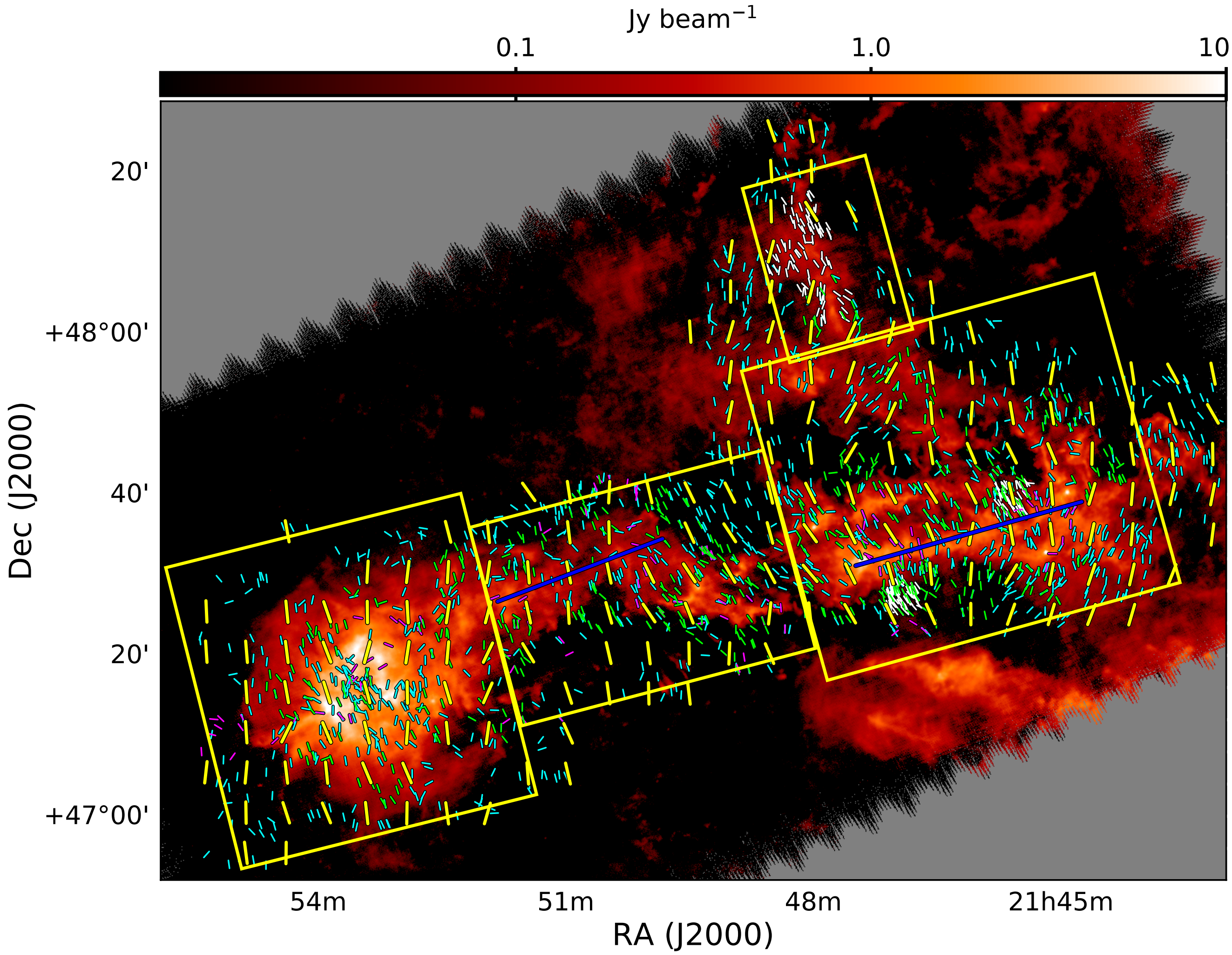


**Figure 5.** The stellar polarization map overlaid on the *Herschel* 250 $\mu$m map. The detection in $i'$, $R_c$, $H$, and $K$ bands are show with white, green, cyan, and magenta vectors. The yellow vectors are the spatially averaged H band polarization detection. The yellow boxes label the four sub-regions in different evolutionary stage. The blue lines are the filament ridges which we used to calculate the radial distance in

PA systematically increase from -10°at radial distance of -15 arcmin to 20° at a radial distance of 5 arcmin, and then back to -20° when the radial distance is greater than 20 arcmin. The magnetic field is perpendicular to the main filament within 10°when the radial distance is between 0–20 arcmin, but the PA shows a $\sim 30°$ offset to the filament orientation when the radial distance is $< 0$ or $> 20$ arcmin. This features is consistent with the large scale curvature seen in the polarization map, and likely caused the higher PA dispersion.

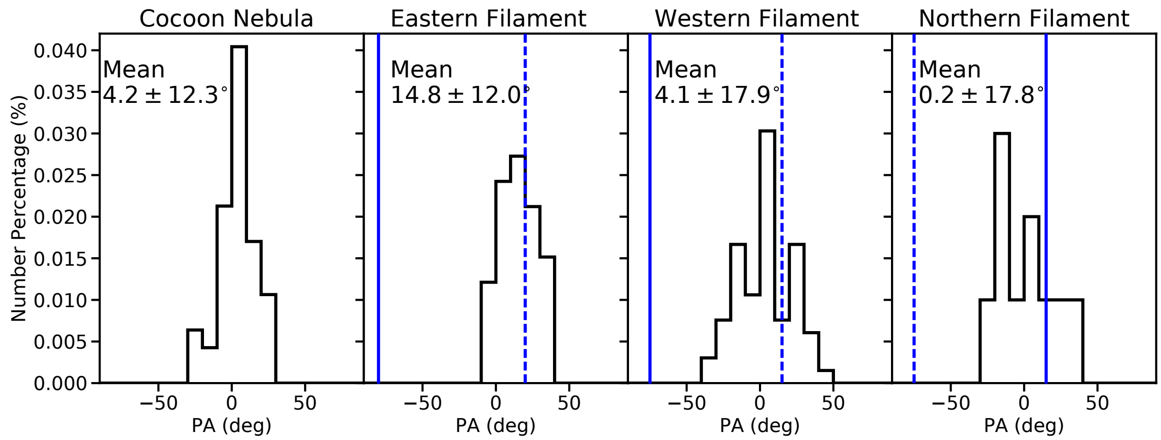


**Figure 6.** The histogram of the smoothed H band polarization PA toward the four sub-regions shown in Figure 5. The blue solid and dashed lines show the orientations parallel and perpendicular to the main filament, respectively. The mean magnetic field orientation in these four sub-regions are similar within $sim10^{\circ}$, and the angular dispersion of $sim12^{\circ}$ in the eastern side is lower than the angular dispersion of $sim18^{\circ}$ in the western side.

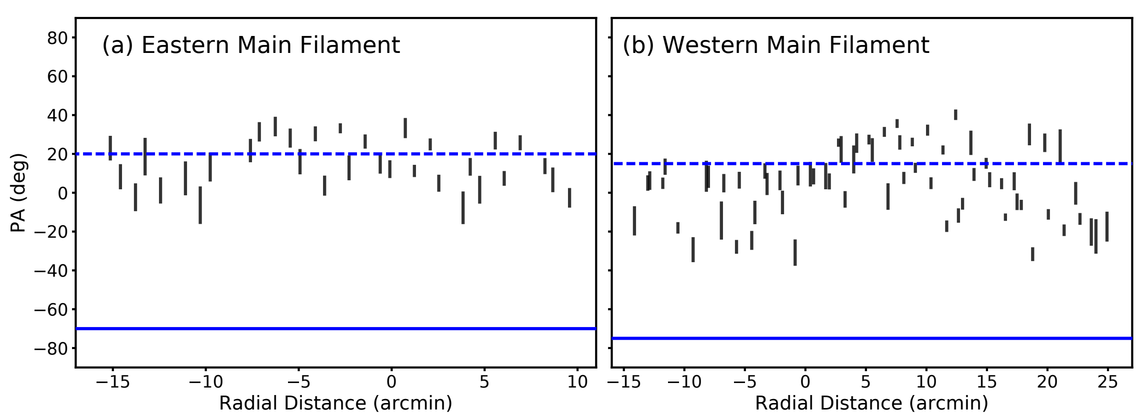


**Figure 7.** The polarization PA vs. the radial distance to the filament ridge. The black lines show the spatially averaged H band polarization vectors. The blue solid and dashed lines show the orientations parallel and perpendicular to the main filament, respectively. (a) The magnetic field is mostly perpendicular to the eastern main filament, and the alignment seems to be not correlated with the radial distance. (b) The magnetic field orientation systematically vary from $\sim 20^{\circ}$ to $\sim 0^{\circ}$ as radial distance changes from 5–20 to $< 0$ and $> 20$ arcmin, where the magnetic field becomes slightly misaligned to the main filament.

### 2.3. *Magnetic Field Strength over the IC5146 Cloud*

The Davis-Chandrasekhar-Fermi (DCF) method (Davis & Greenstein 1951; Chandrasekhar & Fermi 1953) is commonly used to estimate the strength of the plane-of-sky component of the magnetic field ($B_{pos}$) using dust polarization data. Assuming that the turbulent kinematic energy and the turbulent magnetic energy are in equipartition, the DCF method suggests that $B_{pos}$ could be estimated using

$$B_{pos} = Q\sqrt{(4\pi\rho)}\frac{\sigma_v}{\delta\phi}; \delta\phi \leq 25^{\circ}, \tag{1}$$

where $\delta\phi$ is the dispersion of measured polarization orientation, $\sigma_v$ is the line-of-sight velocity dispersion, $\rho$ is the gas density, and $Q$ is a modification factor to correct the overestimation of $B_{pos}$ due to the complicity of the magnetic field structure along the line of sight. Ostriker et al. (2001) found $Q = 0.5$ yielding a good approximation based on their MHD simulation if magnetic field angular dispersion is less than 25°.

#### 2.3.1. *Polarization Angular Dispersion*

To apply the DCF method, we estimated the polarization angular dispersion across the IC5146 cloud. The DCF method assumes that the magnetic field angular dispersion is only contributed from turbulence; however, the reality magnetic fields often have nonuniform geometry in large scale. To remove the large scale PA pattern, we used $6 \times 6$ arcmin bin grid to calculate the local mean polarization PA and the corresponding angular dispersion. The bin size was chosen to ensure enough stars with high S/N were used in the dispersion calculation. The grid-based calculation ensures that each polarization detection was used in only one bin, so that the estimations among bins are independent.

The stars with high S/N (Usage Flag =1) selected in Paper I were used to calculate the angular dispersion. The angular dispersions were calculated using the $R_c$, $i'$, and $H$ data separately, because they may trace different part of the clouds. The standard deviation of the PA distribution was calculated in each bin as the observed angular dispersions ($\delta\phi_{obs}$) and the mean instrumental uncertainties ($\delta\phi_{ins}$) were removed from the $\delta\phi_{obs}$ to obtain the intrinsic polarization angular dispersion ($\delta\phi_{intrinsic}$)

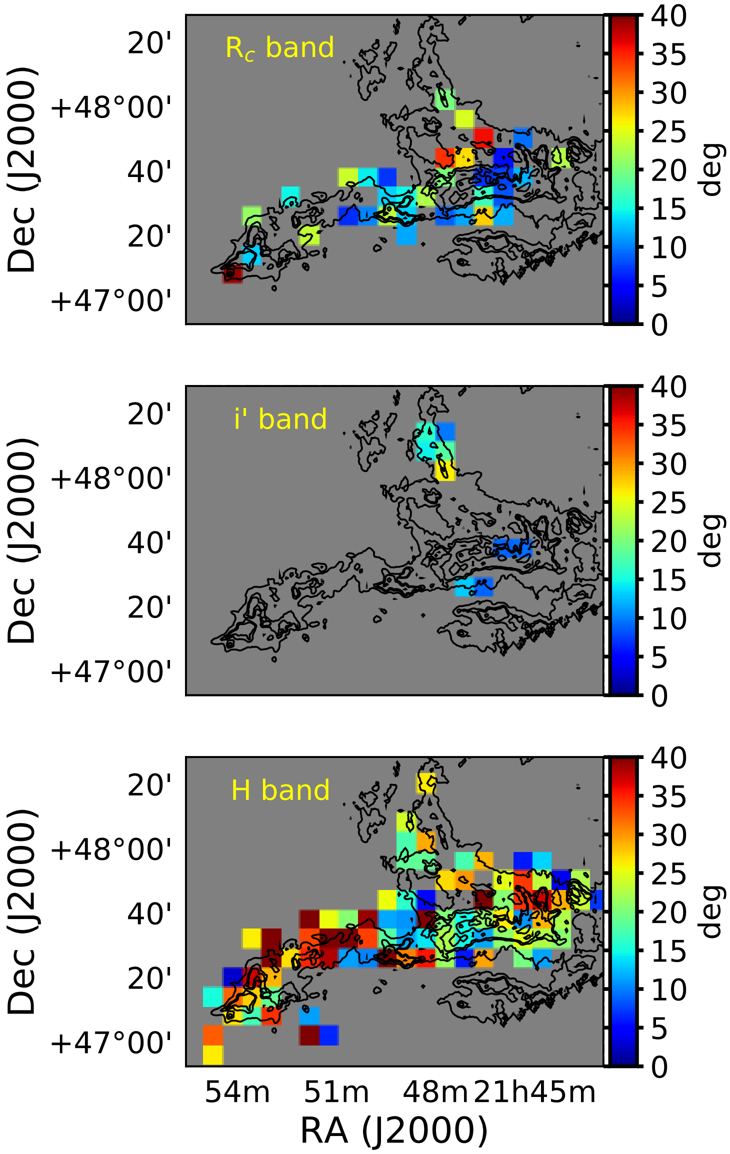


**Figure 8.** The PA dispersion map for $R_c$, $i'$, and $H$ band data, calculated using $6 \times 6$ arcmin pixels. The black contours are the *Herschel* 250 $\mu$m intensities with levels of 0.1, 1, and 5 Jy/beam.

via

$$\delta\phi^2_{intrinsic} = \delta\phi^2_{obs} - \delta\phi^2_{ins}. \tag{2}$$

The final angular dispersion map is shown in Figure 8. The mean uncertainties in angular dispersion is 1.°6, 0.°9, and 3.°2 for $R_c$, $i'$, and $H$ band. The mean S/N of the detected angular dispersion is 11.4, 17.4, and 7.7 for for the $R_c$, $i'$, and $H$ band.

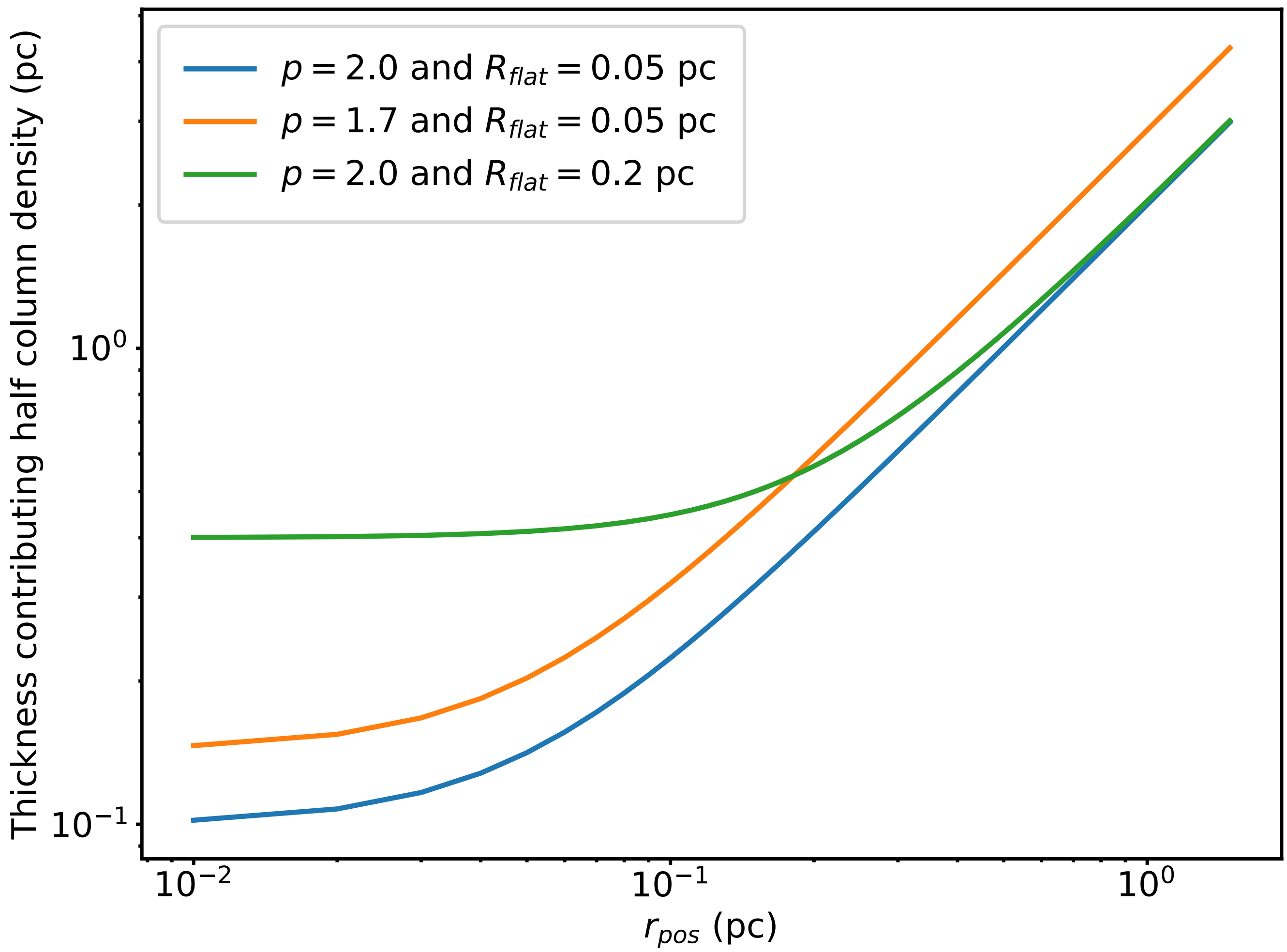


**Figure 9.** The FWHM thickness of plummer-like profile defined in Equation 4. $r_{pos}$ represents the projected radius on the plane of sky. The FWHM thickness is approximately proportional to $r_pos$ if $r_pos >> R_{flat}$.

### 2.3.2. *$H_2$ Volume Density*

The IC5146 cloud consists of numerous filamentary clouds. Arzoumanian et al. (2011) identified 27 filaments in this system based on the *Herschel* data, and showed that the density structure of these filaments could be well described by the plummer-like profile:

$$n_p(r) = \frac{n_c}{[1 + (r/R_{flat})^2]^{p/2}} \tag{3}$$

where $n_c$ and $n_p(r)$ are the $H_2$ volume density at filament ridge and at a radial distance of r to the filament ridge.

To estimate the mean volume density along the line of sight, a cloud boundary is required; however, the plummer-like profile describes a structure extending to infinite $r$, and thus provides no well-defined boundary. Hence, here we defined a half-thickness (D) of a plummer-like structure as the thickness of the central regions that contributes half of the total column density giving

$$\frac{N(D)}{N_{total}} = \frac{\int_{\frac{-D}{2}}^{\frac{D}{2}} n_p(r) dr_{los}}{\int_{-\infty}^{\infty} n_p(r) dr_{los}} = \frac{1}{2}, \tag{4}$$

where $r_{los}$ is the line of sight component of the radial distance. Figure 9 shows how the half-thickness (D) varies with the plane of sky component of the radial distance ($r_{pos}$) for various $p$ and $R_{flat}$. The half-thickness is approximately proportional to $r_{pos}$ when $r_{pos} >> R_{flat}$. The mean volume density along the line of sight could be estimated by

$$\overline{n} = \frac{N_{obs}}{2D}, \tag{5}$$

where $N_{obs}$ is the observed total column density.

For the 27 filaments identified in Arzoumanian et al. (2011) with their fitted Plummer parameters, we calculated the half-thickness for the pixels around each of the 27 filaments, assuming these filaments are cylindrical with a Plummer-like density profile. The half-thickness of each filament was only calculated up to $r_{pos} = \pm 2.3$ pc, which was the boundary used in Arzoumanian et al. (2011) to fit the Plummer model.

In order to determine the thickness of the pixels that are close to multiple filaments, we assumed that the neighboring filaments on the plane of sky were also neighboring along the line of sight, and so they were spatially overlapped. Among the thicknesses calculated from the nearby filaments, we only adopted the lowest one to represent the thickness of that pixel, because lower thickness indicates higher mass concentration and so the corresponding filaments are the major mass contributor of that pixel. Nevertheless, we note that because the real 3D distribution of the filaments is unknown, our thickness estimation could be underestimated if the neighboring filaments are distant and separated along the line of sights.

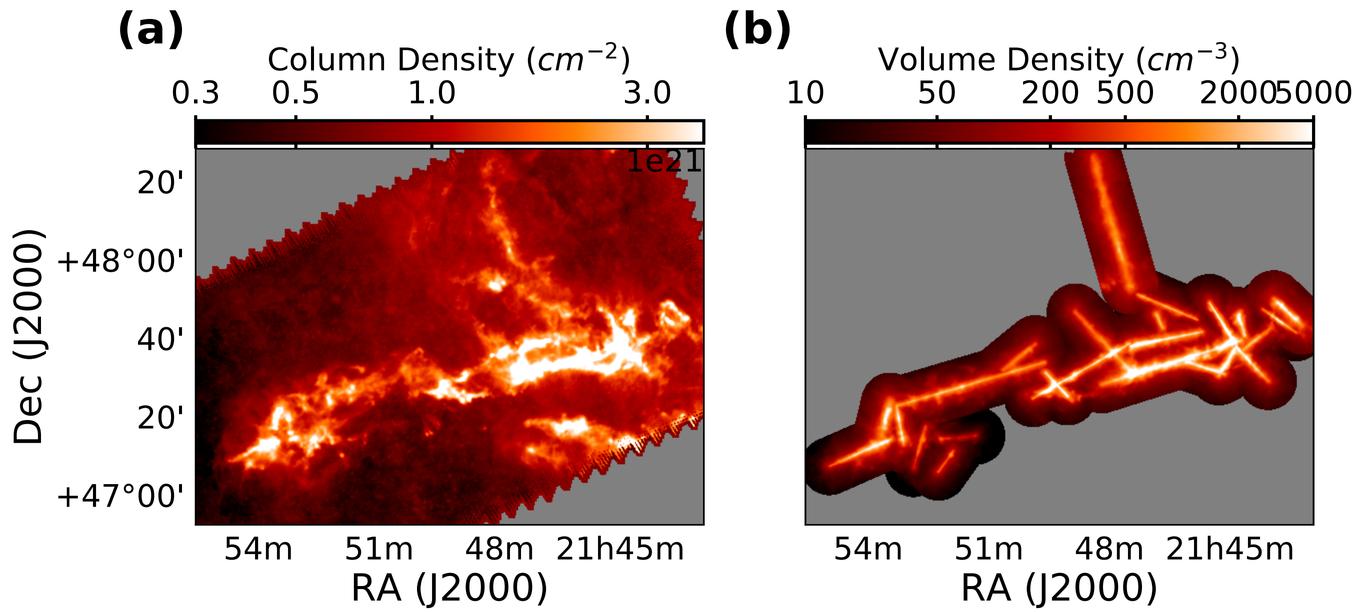


**Figure 10.** (a) The column density map for the IC5146 cloud, calculated in (Arzoumanian et al. 2011) using *Herschel*data. (b) The volume density map estimated by the column density map and the plummer FWHM width (Equation 3).

With the estimated thickness, we used the column density map (Figure 10(a)) in Arzoumanian et al. (2011) calculated from the *Herschel* five bands data to estimate the mean volume density along the line of sight following Equation 5, and the mean volume map is shown in Figure 10(b).

In order to estimate the mean volume density that matches the angular dispersion calculated in $6' \times 6'$ bin grid, we further calculated the mean volume density using the same $6' \times 6'$ grid. Because we used rather big bins, some of the bins might cover both the diffuse region and the dense filament ridge; however, our data can only trace the former. Hence, to obtain the mean density of the regions that our data can really trace, we selected the pixels in Figure 10(b) where we have $R_c$, $i'$, or $H$ band polarization detections. Only the selected pixels were used to calculate the mean volume density for the $6' \times 6'$ grid to match the $R_c$, $i'$, or $H$ band data. As a result, we obtained three mean volume density maps corresponding to the $R_c$, $i'$, and $H$ band data.

#### 2.3.3. *Gas Velocity dispersion*

Arzoumanian et al. (2013) measured the $^{13}$CO (2-1), C$^{18}$O (2-1), and $N_2H^+$ (1-0) lines toward several filaments in the IC5146 cloud, and found that these lines show roughly constant non-thermal velocity dispersions of $0.20 \pm 0.06$ km s$^{-1}$, if the column density is $\lesssim 10^{22}$ cm$^{-2}$. Because most of our polarization detections are located in $A_V \lesssim 10$ mag regions, we assume a constant velocity dispersion of 0.20±0.06 km s$^{-1}$ for our magnetic field strength estimation.

### 2.3.4. *Magnetic Strength*

With the above estimated quantities, we calculated the $B_{pos}$ using Equation 1 for each of the $R_c$, $i'$, and $H$ band data sets separately. The magnetic field strength maps are shown in Figure 11; the $R_c$ and $H$ band data mostly trace the main filament regions, while the $i'$ band data only trace the northern regions. The estimated magnetic field strength is ranged from few $\mu$G in diffuse regions to 30 $\mu$G in dense clouds. The median uncertainty of our magnetic field strength estimation are 36%, 34%, and 35% for the $R_c$, $i'$, and $H$ bands.

For those pixels with $\delta\phi > 25°$, the magnetic field strength could not be accurately estimated using Equation 1 due to the very complicate magnetic field morphology, and therefore could only be used as upper limit estimations. About 40% of the pixels have $\delta\phi > 25°$ and thus the magnetic field strength of these pixels are not shown in Figure 11.

## 2.4. *Magnetic Field Strength versus Density*

Whether the cloud collapse is regulated by the magnetic field can be indicated by the dependence of the magnetic field strength on cloud density ($n$). We plot the $B_{pos}$–$n$ in Figure 13 using the estimations based on $R_c$, $i'$, and $H$ band data. We also show the upper limit estimation for the pixels with $\delta\phi > 25°$. It is clear that the $B_{pos}$–$n$ distribution is truncated by the DCF method limitation, which is set by the magnetic field strength for $\delta\phi$=25°. Because the slope of the boundary is 0.5, direct fitting to the truncated data may bias the determination of $B_{pos}$–n power-law index.

To obtain an unbiased observed $B_{pos}$–$n$ relation, a probability density function (PDF) of the observed magnetic field strength considering the truncation due to the DCF method limitation needs to be used. To construct the PDF of the observed magnetic field strength, we follow the procedure

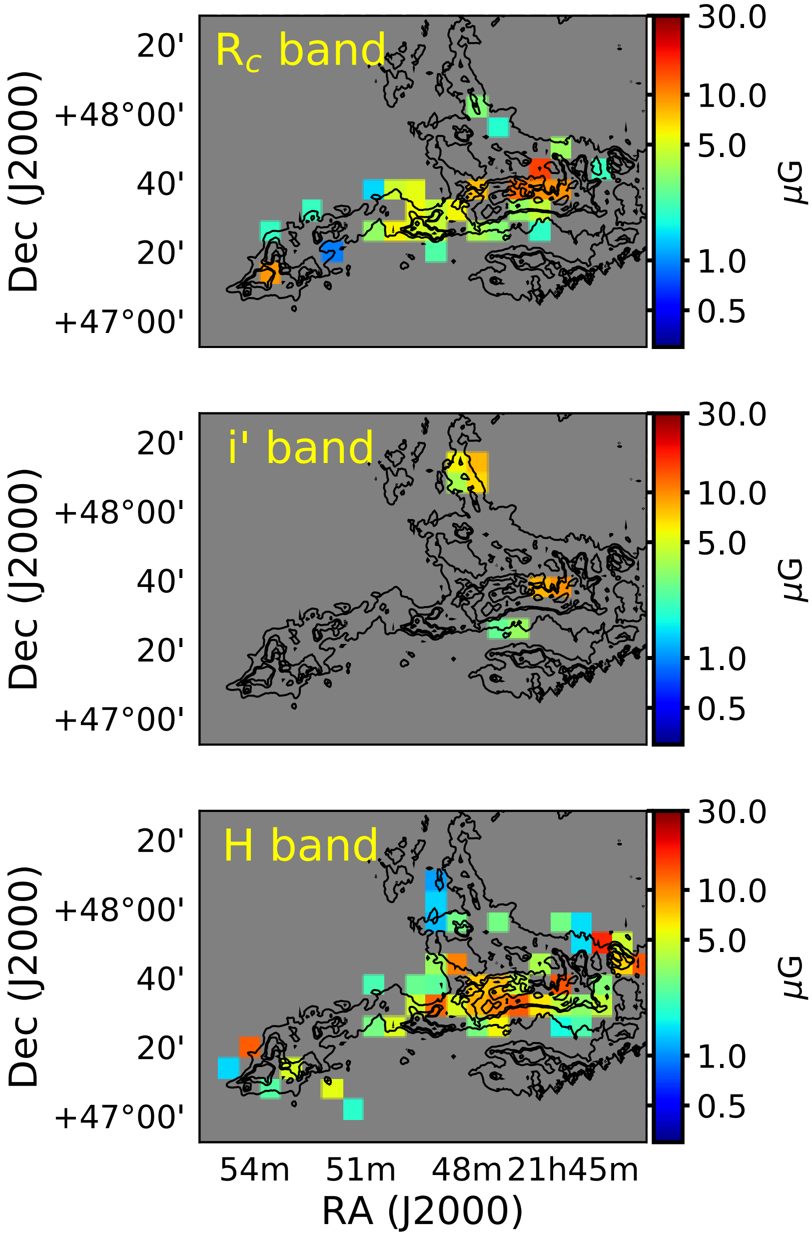


**Figure 11.** The $B_{pos}$ map estimated using the $R_c$, $i'$, and $H$ band data. Only the pixels with PA dispersion $< 25°$ were used to estimate the magnetic field strength. The black contours are the *Herschel* 250 $\mu$m intensities with levels of 0.1, 1, and 5 Jy/beam.

in Crutcher et al. (2010) that describes the PDF of the estimated $B_{pos}$ ($\hat{B}_{pos}$) as the convolution of the observed probability ($P_{obs}$), intrinsic probability ($P_{int}$), and the projection effect ($P_{proj}$):

$$\begin{aligned} P(\hat{B}_{pos}|B) = \int P_{obs}(\hat{B}_{pos}, B_{pos}) \times P_{proj}(B_{pos}, B) \\ \times P_{int}(B, n) dB_{pos} dB. \end{aligned} \tag{6}$$

We further added a truncation condition to the PDF:

$$P(\hat{B}_{pos}|B) = 0 \qquad (\hat{B}_{pos} < B_{limit}), \tag{7}$$

where the $B_{limit} = Q\sqrt{(4\pi\rho)}\sigma_v/25^\circ$ represents the lowest magnetic field strength that the DCF method can be used. Here we assume that our observation uncertainty is Gaussian, described by

$$P_{obs}(\hat{B}_{pos}, B_{pos}) = G(\hat{B}_{pos}, B_{pos}, \sigma_{obs}) \tag{8}$$

where $G(x, \mu, \sigma)$ denotes the Gaussian function, and $\sigma_{obs}$ is the propagated observational uncertainties. Because we found the large scale magnetic field in the IC5146 cloud is roughly uniform, we assume that the $P_{proj}$ is a delta-function peaked at a projection factor $sin(i) = B_{pos}/B$.

The PDF of the intrinsic magnetic field strength in molecular clouds is, nevertheless, uncertain. Although numerical simulations of turbulence-driven cloud formation suggested a Gaussian-like PDF (Falceta-Gonçalves et al. 2008), Crutcher et al. (2010) found that the uniform PDF is better than, or similarly good as, the Gaussian PDF to describe the observed magnetic field strength measured in the Zeeman surveys. However, the samples in Crutcher et al. (2010) are from numerous clouds, and hence it is still unclear whether the uniform PDF is caused by random inclination, cloud intrinsic properties, or cloud diversity. Hence, we tried to use both Gaussian and uniform PDF to perform model fitting, and tested which PDF can better explain our results.

#### 2.4.1. *Gaussian PDF*

Assuming the intrinsic magnetic field strength has a Gaussian PDF:

$$P_{int}(B, B_m) = G(B, B_m, \sigma_{int}), \tag{9}$$

where $\sigma_{int}$ is the intrinsic dispersion of the magnetic field strength, and $B_m$ is given by the $B$–$n$ model in Crutcher et al. (2010):

$$B_m(n, \theta) = \begin{cases} B_0 & n < n_0 \\ B_0(n/n_0)^\alpha & n > n_0, \end{cases} \tag{10}$$

where $\theta$ denotes the free model parameter, including $B_0$, $n_0$, and $\alpha$. Since the convolution of two Gaussian PDFs is still a Gaussian, Equation 6 could be simplified to a simple Gaussian, and becomes a truncated Gaussian if the truncation condition is applied. Figure 12 illustrates an example of a truncated Gaussian PDF. The likelihood function of the observed $B_{pos}$ becomes

$$P(\hat{B}_{pos}|\theta) = \begin{cases} \frac{G(\hat{B}_{pos}, B_m(n,\theta), \sigma_{con})}{\sigma_{con}(1-\Phi(B_{min}, B_m(n,\theta), \sigma_{con}))} & B_{min} < \hat{B}_{pos} \\ 0 & \hat{B}_{pos} < B_{min}, \end{cases} \tag{11}$$

where $\sigma^2_{con} = \sigma^2_{obs} + \sigma^2_{int}$ is the convolved dispersion, $\Phi$ denotes the Gaussian cumulative distribution function, and the $B_{min}$ is the minimum detectable magnetic fields strength, which is set by Equation 1 with $\delta\phi = 25°$. We note that we used distinct observational uncertainties $\sigma_{obs}$ for each of the data points, and hence the convolved Gaussian width is not a constant.

According to the Bayesian theorem, we could fit the observed data via

$$P(\theta|D) = \frac{P(D|\theta)P(\theta)}{P(D)}. \tag{12}$$

$P(\theta|D)$ (posterior) provides the PDF of the model parameter, which is what we want to know. $P(D|\theta)$ is the likelihood function as shown in Equation 11, $P(\theta)$ is our prior guess of the model parameter, and P(D) is the distribution of data, which is merely a constant to normalize the probability function.

We performed a model fitting using the Python PyMC3 Package (Salvatier et al. 2016) via Markov Chain Monte Carlo (MCMC) method using the No-U-Turn sample algorithm (Hoffman & Gelman 2014). To enhance the MCMC converge efficiency, we chose the priors with a half Gaussian PDF, instead of an uniform PDF:

$$\begin{cases} P(\alpha) & = HalfGaussian(\sigma = 1) \\ P(n_0) & = HalfGaussian(\sigma = 5) \\ P(B_0) & = HalfGaussian(\sigma = 50) \\ P(\sigma_{int}) & = HalfGaussian(\sigma = 0.5). \end{cases} \tag{13}$$

We note that the choice of priors only have little effects on the fitting results, since we provide sufficient data to constrain the model. We used this model to generate 60000 samples to explore

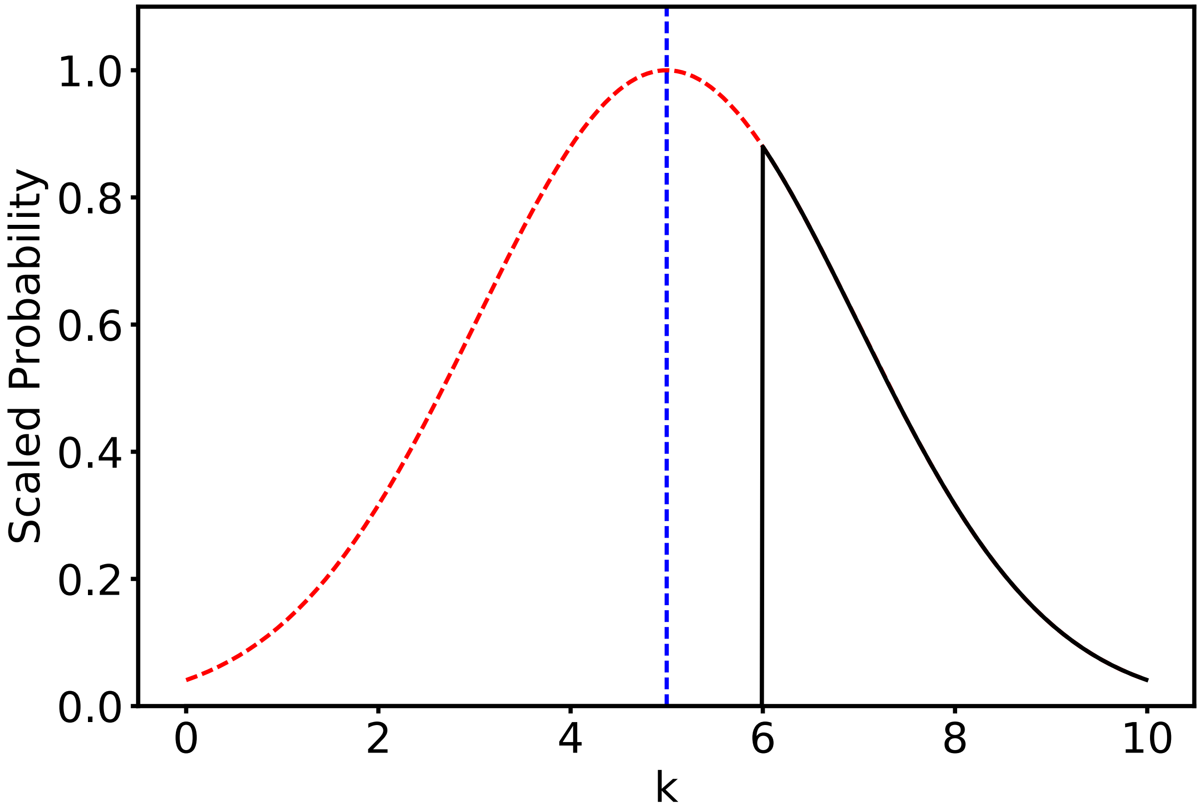


**Figure 12.** An example of truncated Gaussian distribution. The red dashed line shows a Gaussian with $\mu = 5$ (blue dashed line) and $\sigma = 3$. The black line show the same Gaussian distribution truncated by a lower boundary of 6. The peak probabilities of these two PDF are both scaled to 1 to emphasize the different shape. Depending on the truncated boundary, the most probable value ($\mu$) of the original PDF is not necessary covered by the truncated PDF.

the parameter space, and the first 10000 samples were removed to avoid the non-converged sample, which may be correlated with our chosen initial guess.

The PDF of each model parameter is shown in Figure 14. We obtained an $\alpha$ of 0.44 with a 95% confidence interval from 0.41 to 0.47, which is significantly lower than the $\alpha$ of 0.66, predicted by the isotropic collapse model, and thus suggest that the magnetic field may be important in regulating the collapse of the IC5146 cloud.

Figure 13 shows the comparison between our data and the intrinsic $B$–$n$ distribution predicted by the posterior. We note that the observational uncertainties is not included in the plotted prediction,

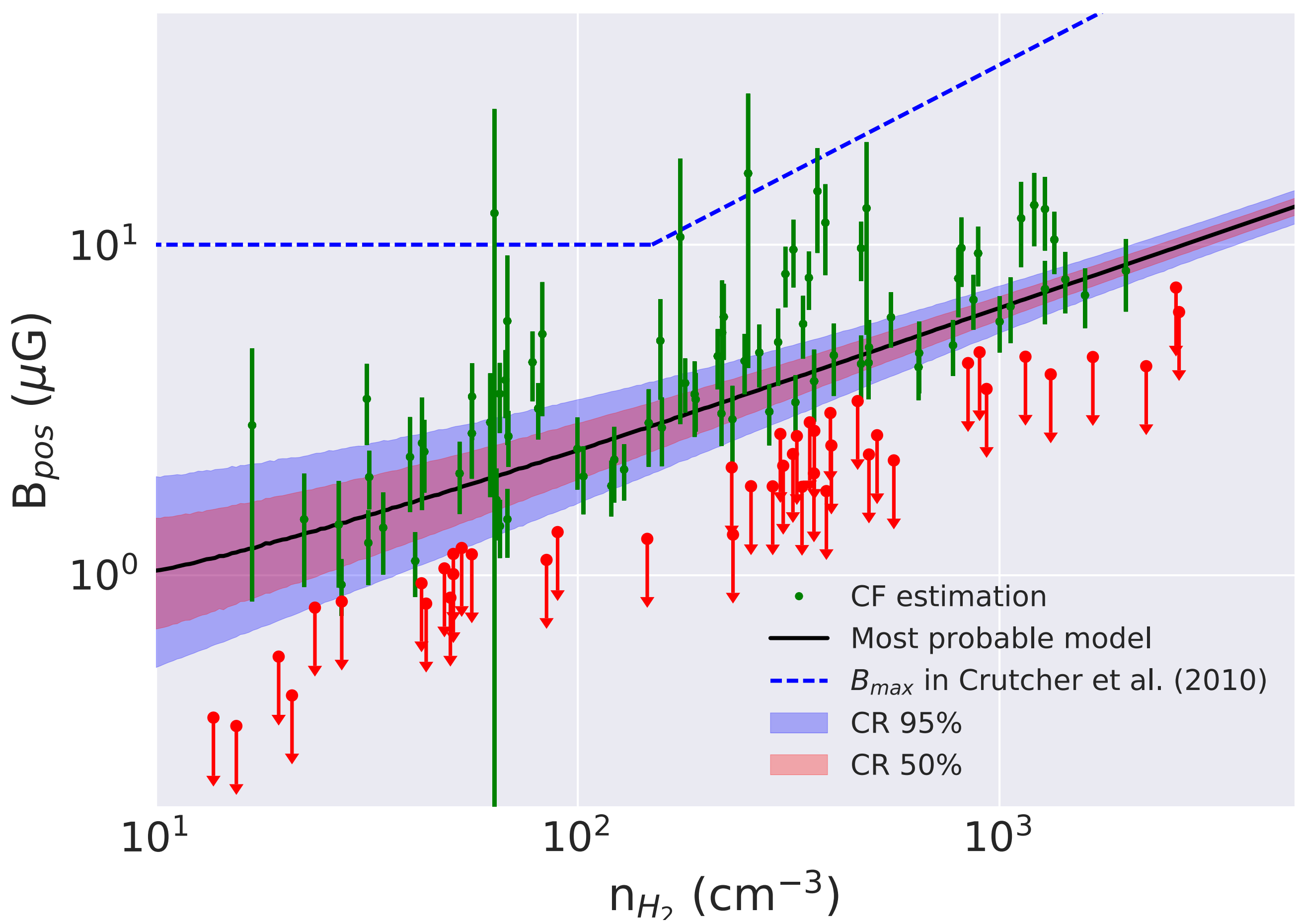


**Figure 13.** $B_{pos}$ versus volume density. The green points represent the $B_{pos}$ and volume density of the pixels shown in Figure 11. The red points show the results obtained from the pixels with PA dispersion greater than 25°, which shows that about 40% of our samples cross the limitation of the DCF method. The black line represents the mean posterior prediction from our Bayesian analysis using a Gaussian PDF model, and the colored regions show the 50% and 95% confidence region of the posterior prediction. This prediction does not include observational uncertainties, since observational uncertainties are distinct point by point. The blue dashed lines are the maximum magnetic field strength obtained in Crutcher et al. (2010), which shows an different slope of 0.66.

since the observational uncertainties varies data by data. The 95% confidence regions seem to be consistent with our data. The best fitted $\alpha$ is 0.48 with a 95% highest posterior density (HPD) ranged from 0.43 to 0.53. The $n_0$ is 6 cm$^{-3}$ with a 95% HPD ranging from 1 to 16, which is much lower than the previous results of hundred cm$^{-3}$, possibly because we have only a few estimations in such diffuse regions to constrain the flat part.

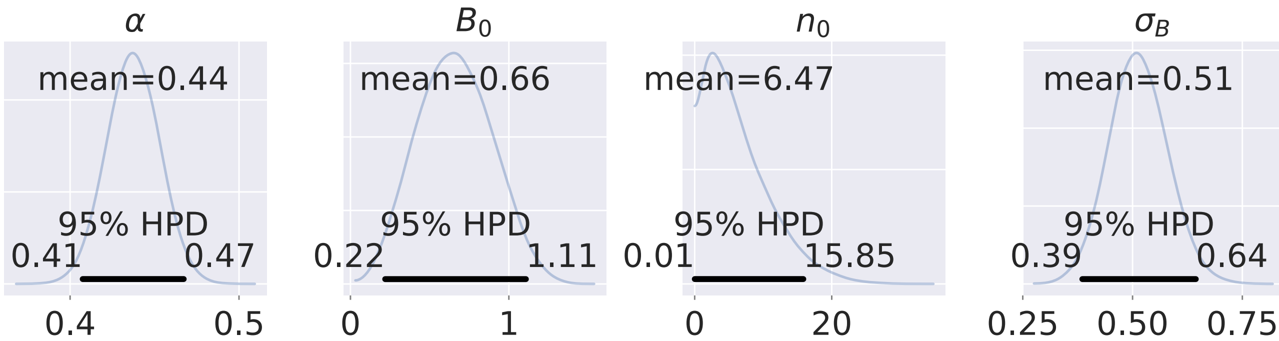


**Figure 14.** PDFs of each of the four parameters in the Bayesian model fitting using truncated Gaussian likelihood. The mean and 95% highest posterior density (HPD) interval are labeled for each parameter.

Figure 15 shows the pairwise plots among the four parameters referred in our Bayesian analysis. Values of $\alpha$ do not seem to be strongly correlated with values of $n_0$ and $B_0$. This suggests that even the real $B_0$ or $n_0$ is higher than what we derived, values of $\alpha$ would not be changed significantly.

### 2.4.2. *Uniform PDF*

In addition to the Gaussian PDF, we also tested the model assuming that the intrinsic magnetic field strength follows an uniform PDF (see Figure 16) with

$$P_{int}(B, B_{max}) = \begin{cases} \frac{1}{B_{max}}, & B < B_{max} \\ 0 & otherwise, \end{cases} \tag{14}$$

where $B_{max}$ is the maximum magnetic field strength, which we assumed following the same model as the $B_m$ in Equation 10. The likelihood function of the observed $B_{pos}$ becomes the convolution of a Gaussian and a uniform function:

$$P(\hat{B}_{pos}|\theta) = \begin{cases} \int \frac{G(\hat{B}_{pos}, B, \sigma_{obs})}{B_{max}} dB & \hat{B}_{pos} < B_{max} \\ 0 & otherwise. \end{cases} \tag{15}$$

We note that the uniform PDF models used in Crutcher et al. (2010) include a lower boundary $fB_{max}$; however, because of the limitation of the DCF-method, we do not have the low magnetic field strength samples to constrain the lower boundary of the intrinsic magnetic field strength. Hence, our model neglects the lower boundary term, and the model is only determined by the upper boundary

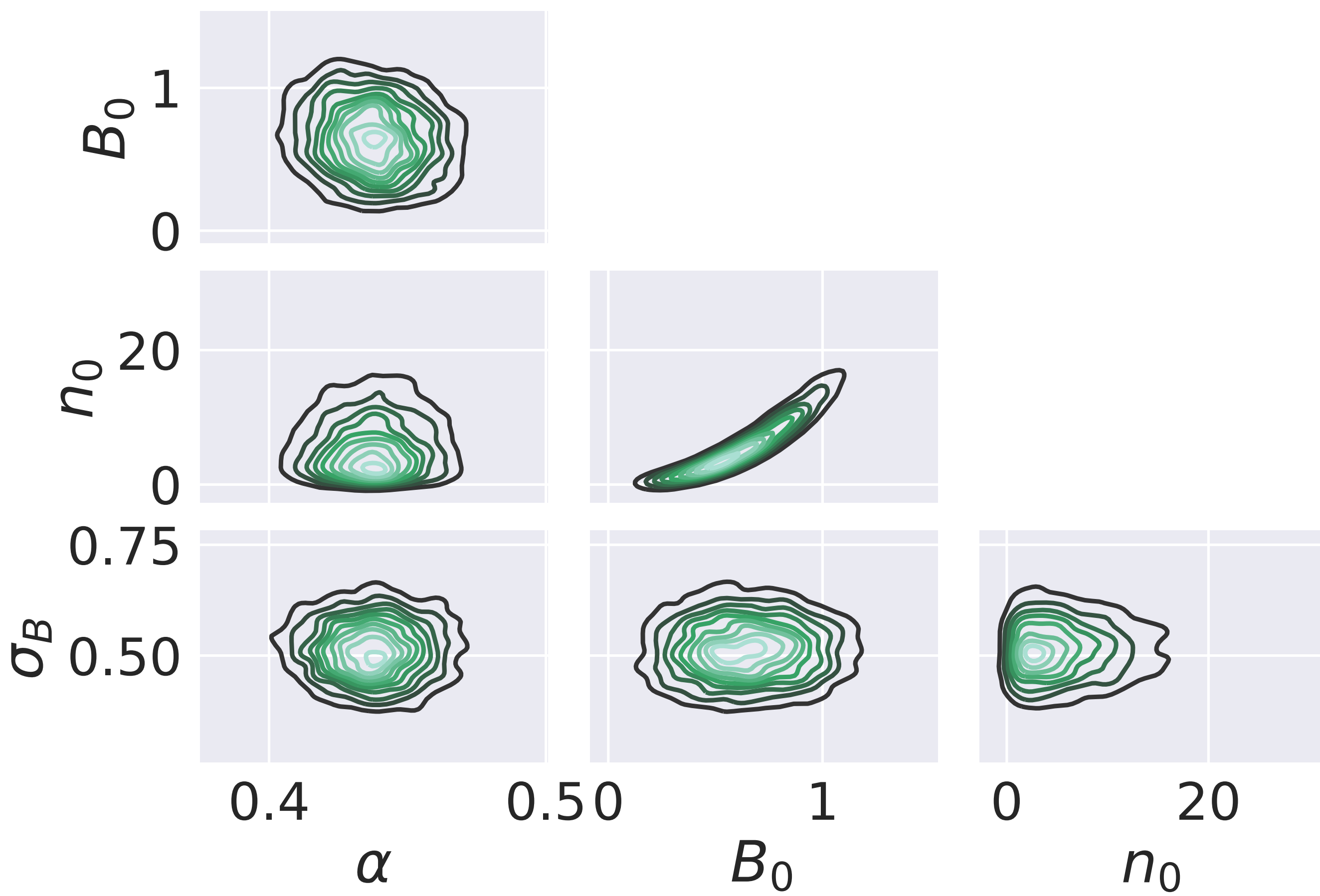


**Figure 15.** Correlations between the model parameters. The $\alpha$ is roughly proportional to $n_0$. If $n_0$ approaches 150 cm$^{-3}$, $\alpha$ could become $\sim$0.6.

of the $B$–$n$ distribution ($B_{max}$). Our choice of priors were

$$\begin{cases} P(\alpha) & = HalfGaussian(\sigma = 1) \\ P(n_0) & = HalfGaussian(\sigma = 5) \\ P(B_{max}) & = HalfGaussian(\sigma = 50). \end{cases} \tag{16}$$

Similar to the Gaussian PDF model, we performed the model fitting in Bayesian interface using the MCMC method with the No-U-Turn sample algorithm. The PDF of each model parameters are shown in Figure 18. The fitted $\alpha$ is 0.42 with 95% HPD ranging from 0.27 to 0.58, which is very similar to the $\alpha$ of 0.44 obtained from the Gaussian PDF model. The fitted $n_0$ is 38 cm$^{-3}$ with a 95% HPD ranged from 0 to 87. The fitted $B_{max}$ is $\sim$2 $\mu$G, which is lower than the $B_{max}$ of $\sim$10

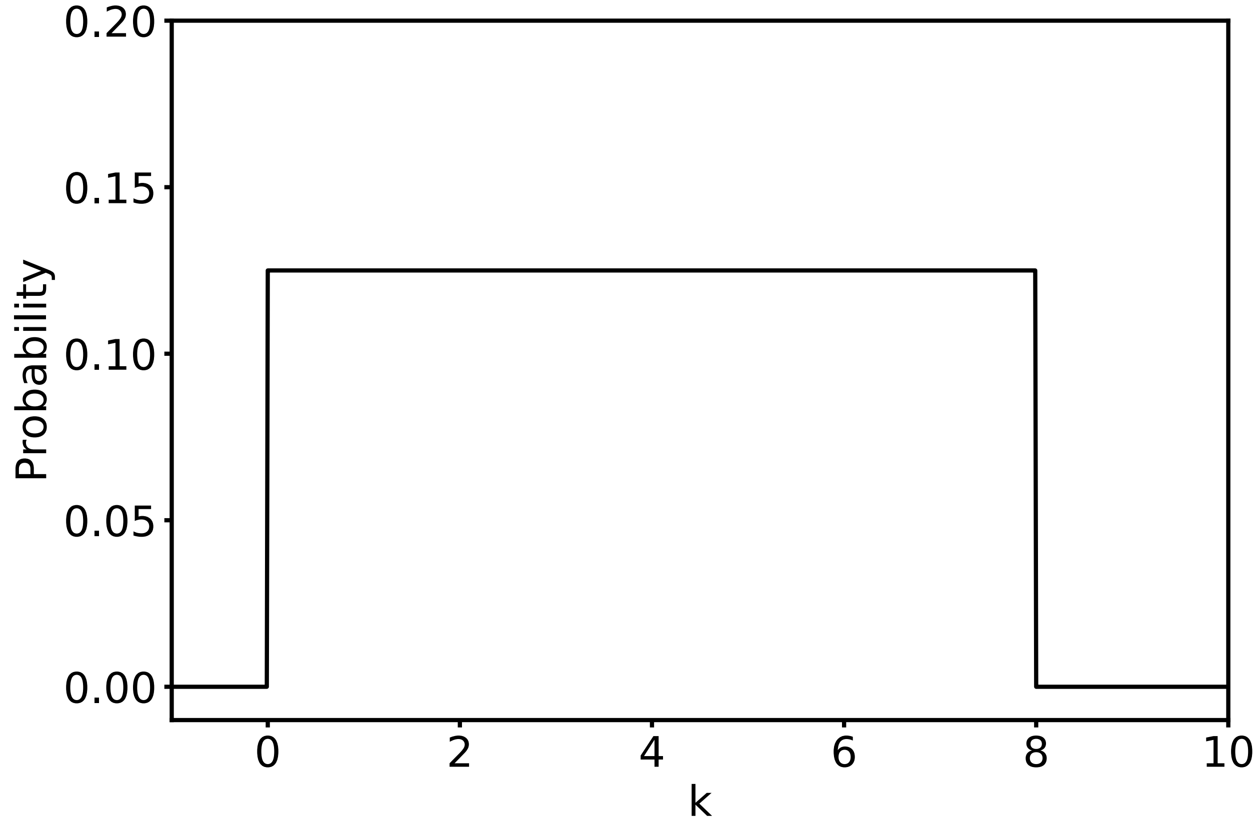


**Figure 16.** An example of uniform PDF. The black line shows an uniform distribution with a upper bound of 8.

$\mu$G estimated in Crutcher et al. (2010). Since Crutcher et al. (2010) uses the data from numerous clouds, their samples likely consist of magnetic fields of all possible inclination angles, and thus their $B_{max}$ possibly represents the total magnetic field strength. In contrast, what we measured is the maximum $B_{pos}$ from a cloud with a roughly uniform magnetic field. If we assume that the $B_{max}$ derived in Crutcher et al. (2010) is a universal value for the diffuse clouds, the lower maximum $B_{pos}$ could be caused by the projection of $sin(i) = B_{pos}/B_{total} \sim 0.2$, implying an inclination angle of $\sim 12°$ with respect to the line of sight. Nevertheless, we cannot exclude the possibility that the magnetic field in IC5146 cloud is weaker than the Crutcher et al. (2010) samples.

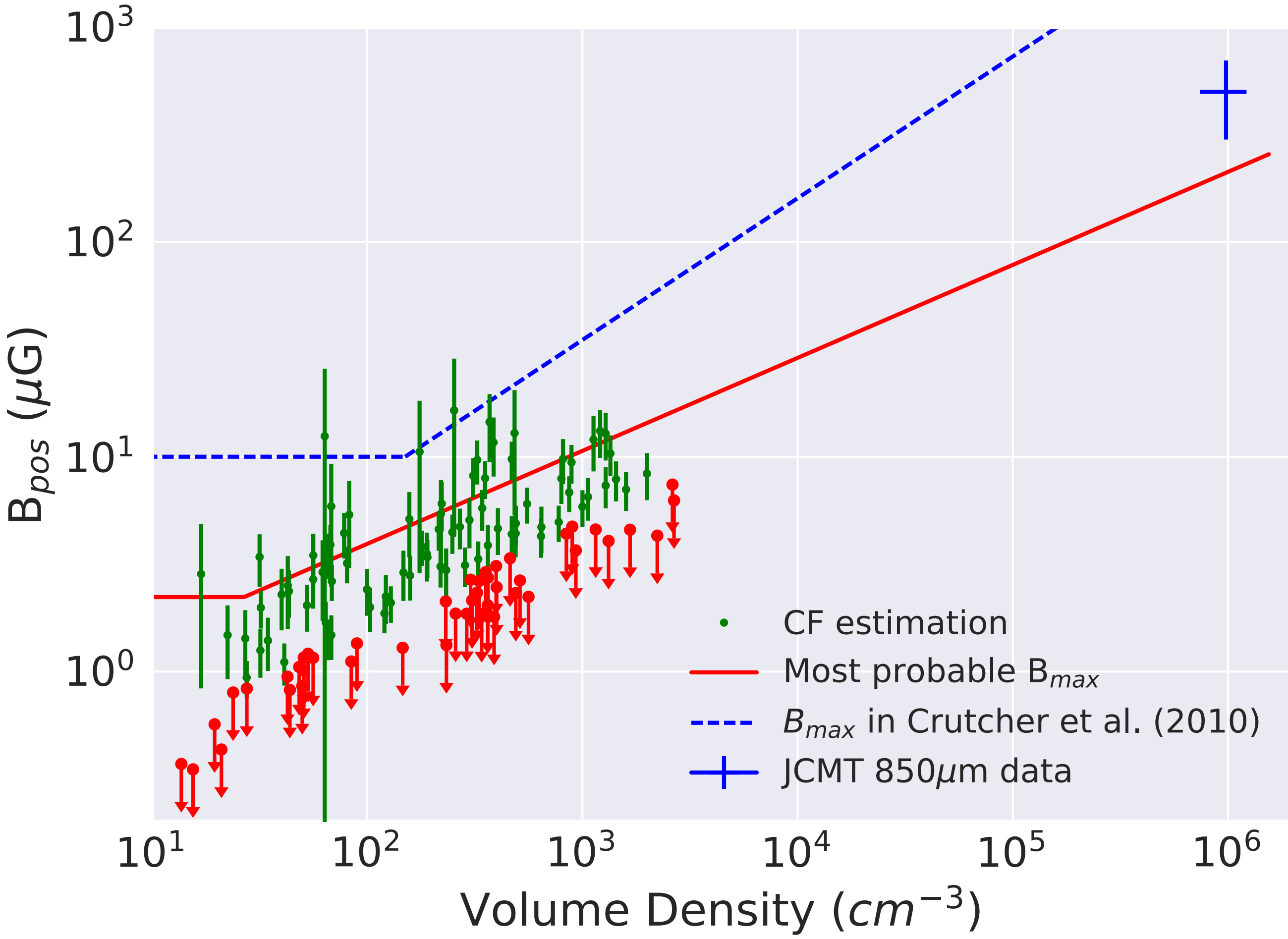


**Figure 17.** Same us Figure 13, but the red line represent the maximum magnetic strength obtained from our Bayesian model using an uniform likelihood. The blue points label the $B_{pos}$ and volume density toward one of the dense hub-filament system in the IC5146 cloud using JCMT 850 $\mu$m polarization data (Wang et al. 2019).

Figure 19 shows the pairwise plots among the three parameters referred in our Bayesian analysis. Values of $\alpha$ seems to be weakly anticorrelated with values of $B_{max}$ and show no correlation with $n_0$. The value of $\alpha$ is always less than 0.5, unless the real $B_{max}$ is extreme small ($< 1$ $\mu$G).

In order to test which PDF can better describe the intrinsic magnetic field strength, we used the Pareto-Smoothed Importance Sampling (PSIS) Leave-One-Out (LOO) cross-validation to examine the accuracy of our fitting. LOO cross-validation selects one of the data point as a testing sample to validate the fitting results obtained from the rest of data in each iteration, and repeats the procedure until all data points are used as test samples. An error rate could be estimated from the Loo cross-

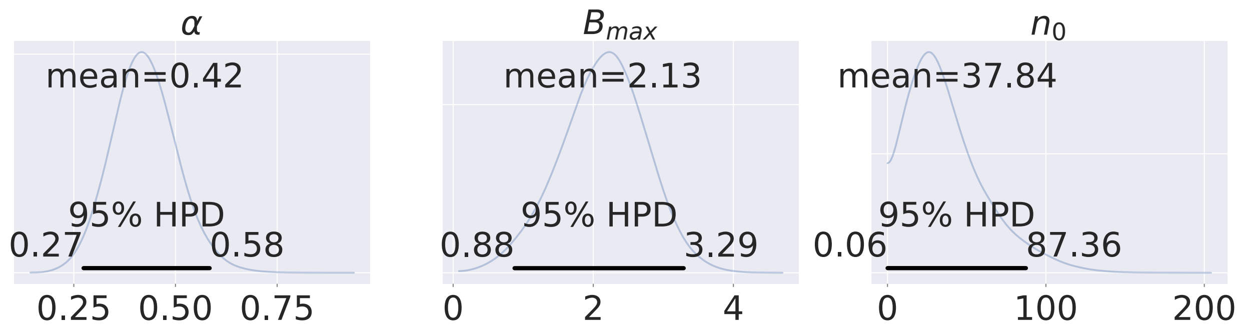


**Figure 18.** PDFs of each of the three parameters in the Bayesian model fitting using uniform likelihood. The mean and 95% highest posterior density (HPD) interval are labeled for each model parameter.

validation to evaluate the goodness of the model, and an lower error rate indicates a better model. Vehtari et al. (2017) proposed an efficient approach to perform the LOO cross-validation using the posterior distribution obtained in a Bayesian model based on the PSIS algorithm. Using the PSIS-LOO validation, we estimated an error rate of 1811±52 and 294±18 for our Gaussian and uniform PDF models. Hence, we conclude that the uniform PDF can better explain our results. We note that the goodness of models might also be influenced by the information loss due to the data truncation, and thus more evidence is still needed to confirm the intrinsic magnetic field strength PDF is uniform.

### 2.4.3. *Mass-to-Magnetic Flux ratio*

The mass-to-flux ratio ($M/\Phi$) of a region indicates the relative importance of the magnetic field and the gravity. The observed mass-to-flux ratio is commonly compared to the critical mass-to-flux value by

$$\left(\frac{M}{\Phi}\right)_{cri} = \frac{1}{2\pi\sqrt{G}} \tag{17}$$

(Nakano & Nakamura 1978), and a critical ratio ($\lambda$) is defined as

$$\frac{(M/\Phi)}{(M/\Phi)_{cri}} = \frac{1}{2\pi\sqrt{G}} \tag{18}$$

(Crutcher 2012), which indicates whether magnetic fields are sufficiently strong to support the gravity. The $M$ and $\Phi$ in this equation refers to the magnetic flux and column density along the

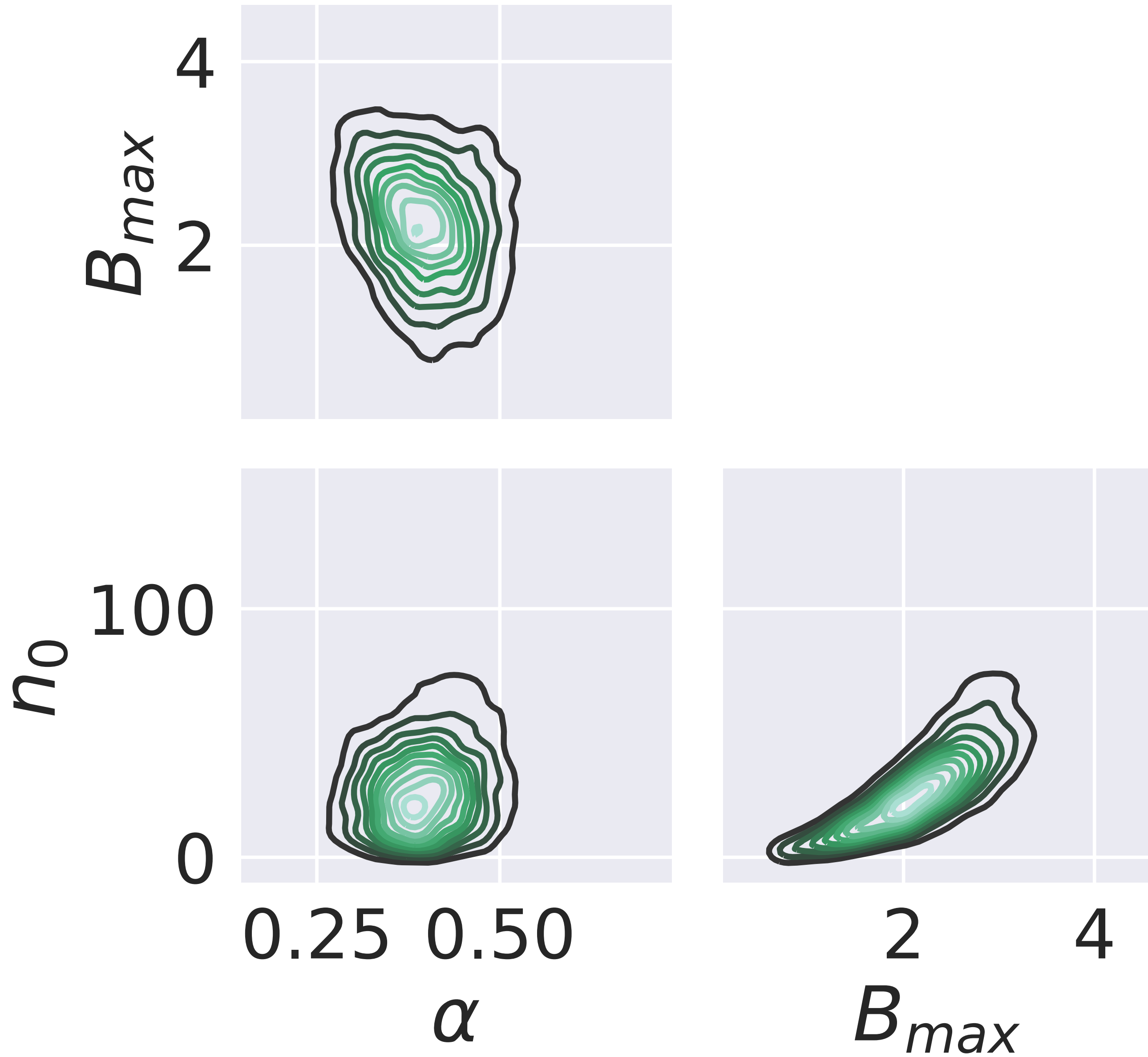


**Figure 19.** Correlations between the model parameters. The $\alpha$ does not seem to correlate with $n_0$, unlike the fitting results using Gaussian likelihood.

magnetic field direction, and hence the observed mass-to-flux ratio ($(M/\Phi)_{obs}$) is expected to be overestimated by a factor of $f$ due to the projection effect as

$$(M/\Phi) = (M/\Phi)_{obs}/f. \tag{19}$$

The factor $f$ depends on the geometry of the clump and magnetic fields. If the cloud long axis is perpendicular to the magnetic field direction, the factor $1/f$ would be $sin(\theta)cos(\theta)$ (Crutcher et al. 2004). If the long axis of a cloud is perpendicular to the magnetic field direction, the factor $1/f$ would be $sin^2(\theta)$ (Crutcher et al. 2004), although this case is only seen in the northern filament region. Assuming a $\theta$ of 12°estimated from the maximum magnetic field strength ( subsubsection 2.4.2), we adopt $f = 5$ to derive the actual mass-to-flux ratio.

We plotted the actual mass-to-flux criticality derived from the $R_c$, $i'$, and $H$ band data in Figure 20. The median uncertainty of the mass-to-flux criticality is 36%. These three maps show how mass-to-flux criticality varies at different depth in the cloud. In the $R_c$ and $i'$ maps, which trace the outer layer of the cloud, most of the regions are magnetically subcriticall ($(M/\Phi)/(M/\Phi)_{cri} < 1$), suggest that the magnetic field is sufficient to support the gravity. In contrast, the $H$ band mass-to-flux criticality map, which traces the inner layer of the cloud, reveals that some of the dense filaments are transcritical ($(M/\Phi)/(M/\Phi)_{cri} \approx 1$) or even supercritical ($(M/\Phi)/(M/\Phi)_{cri} > 1$), and those regions are consistent with the distribution of the YSOc identified in Harvey et al. (2008). These results favor the scenario that the cloud is evolved from magnetically subcriticall condition in the large scale to the supercriticall condition within the dense filaments, where star formation activity takes place.

## 3. DISCUSSION

### 3.1. *Magnetic Field Morphology*

The background starlight polarizations observed towards the IC5416 cloud have revealed detailed information about the magnetic field within and around the cloud. The averaged polarization map further provide a evenly sampled magnetic field morphology at a 0.6 pc scale. In the 0.6 pc scale, the mean polarization angles over the cloud are very similar and the angular dispersion is small ($< 18°$), indicating the overall large scale magnetic field around this cloud is likely uniform. The polarization PA histogram in Figure 6 toward the subregions in this cloud show that the PA dispersions in the western side ($\sim 18°$) are generally higher than the PA dispersions in the eastern side ($\sim 12°$). Figure 7 further revealed that the higher PA dispersions in the western part of the main filament are likely

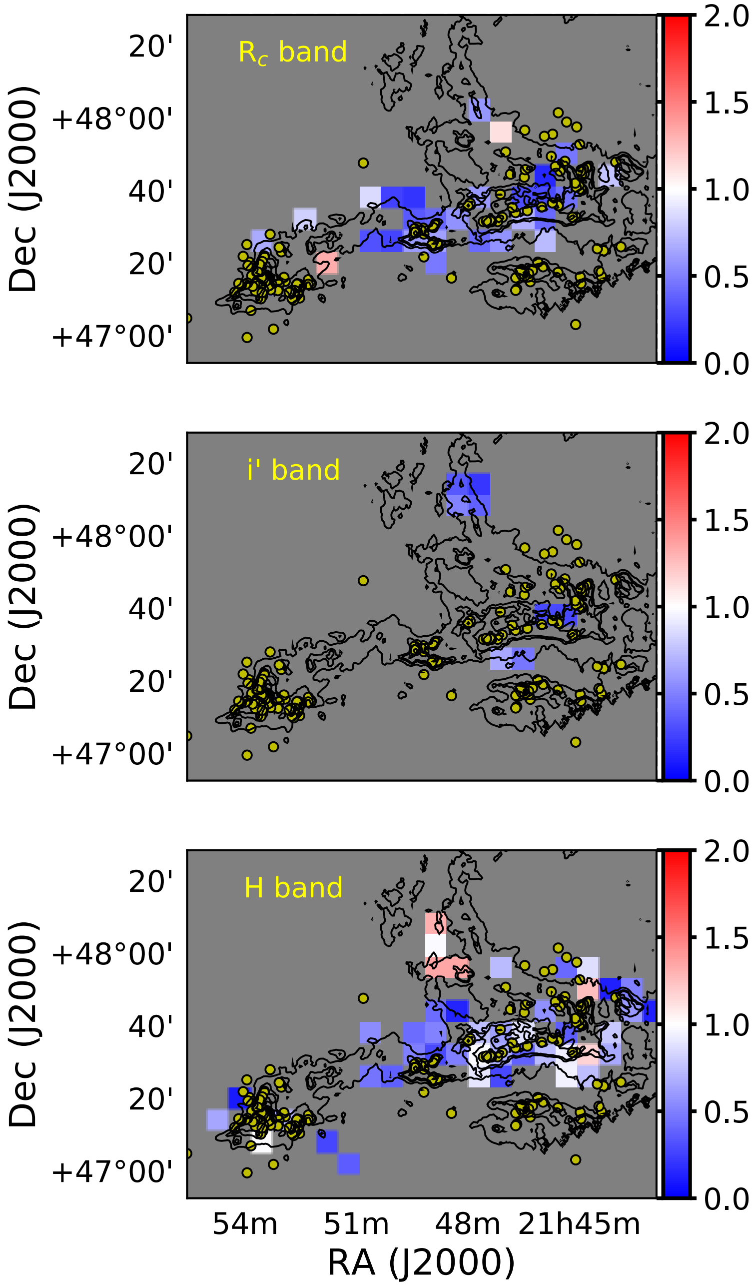


**Figure 20.** The mass-to-flux ratio map over the IC5146 cloud for $R_c$, $i'$, and $H$ band data. The $R_c$ and $i'$ band data, tracing the magnetic fields in the outer part of the cloud, seems to show lower mass-to-flux ratio than $H$ band data. The yellow points label the YSO candidates identified in Harvey et al. (2008). The spatial distribution of YSOs are consistent with the magnetically supercritical regions. The black contours are the *Herschel* 250 $\mu$m intensities with levels of 0.1, 1, and 5 Jy/beam.

caused by the large scale (∼2 pc) magnetic field curvature instead of the smaller scale magnetic field perturbation that is likely related to turbulence or star formation feedback.

Two possibilities could explain the higher PA dispersions found in the western part of the cloud:

(i) The filaments in the western part of the cloud tend to be thermally supercritical so that the thermal energy is insufficient to supprt the gravity (Arzoumanian et al. 2011), and the large scale magnetic fields could be modified by the collapse of the large scale molecular cloud. Gómez et al. (2018) modeled magnetized molecular clouds undergoing global, multi-scale gravitational collapse, and show that the global collapse of molecular clouds may drag the parsec-scale magnetic fields and cause a curvature pattern. The predicted pattern is consistent with the observed curved magnetic field morphology and the broadend PA distribution. In addition, a similar curved pattern has also been observed by the JCMT observations around the sub-parsec scale hub-filament structure embedded in this region (Wang et al. 2019).

(ii) As we have shown in the distance estimation (Section 2.1), the IC5146 cloud is likely consisted by two layers at distances of $\sim 600$ and 800 pc. Since the observed curvature pattern is outside the dense filaments, the polarization possibly traces the magnetic fields in another layer. This possibility is supported by the PA histograms toward the western and norther filament regions, which both show additional peaks at PA$\sim -20^{\circ}$, although these peaks may also be caused by the insufficient number of vectors.

The nearly uniform magnetic fields perpendicular to the filamentary cloud suggest that the cloud is likely formed in a strong magnetic field condition that the filament formation or fragmentation tends to follow the magnetic field direction and hence the magnetic field morphology remains uniform even after the super critical dense filaments are formed (e.g. Nakamura & Li 2008; Van Loo et al. 2014). It is surprising that even the large scale magnetic fields within the HII are still almost uniform, which suggests that the feedback effect is possibly limited in the sub-parsec scale.

### 3.2. *Magnetic Field Strength*

Whether magnetic fields within molecular clouds are sufficiently strong to support gravity and prevent gravitational collapse is a key question in star formation theories. The theories assuming strong magnetic field expect that a molecular cloud is initially magnetically subcritical but gradually becomes supercritical as its density increases through magnetic flux diffusion mechanisms such as ambipolar diffusion (e.g. Mouschovias & Morton 1991), accretion (e.g. Heitsch & Hartmann 2014), turbulent diffusion (e.g. Kim & Diamond 2002), or reconnection diffusion (e.g. Santos-Lima et al. 2010). One observational testable prediction of the strong magnetic field theories is that the mass-to-flux criticality must be subcritical in cloud envelopes, wheresa in cores diffusion mechanisms lead to transcritical or supercritical (Crutcher 2012). In contrast, the theories assuming weak magnetic fields predict supercritical mass-to-flux ratio over the entire molecular clouds.

With our polarization data, we estimated the magnetic field strength and mass-to-flux ratio over the IC5146 cloud. The mass-to-flux ratio estimated using our $R_c$ band data, tracing the diffuse envelope of the cloud, is subcritical over the cloud. In contrast, the mass-to-flux ratio estimated using our $H$ band data, which are able to penetrate the dense part of the cloud, is varying from subcritical in the diffuse regions to supercritical in the dense regions. In addition, these supercritical regions are consistent with the spatial distribution of the known YSOc. These features are consistent with the prediction from the strong magnetic field theories.

### 3.3. *B–n Relation*

How magnetic field strength scales with cloud density provides important information on how the cloud collapse is regulated by magnetic fields and how mass-to-flux ratio increases within clouds. For example, Crutcher et al. (2010) found that the magnetic field strength is scaled with core density by $B \propto n^{0.65}$ for $n_{H_2} > 150$ cm$^{-3}$, suggesting that the core contraction is isotropic and not likely be regulated by magnetic fields. In addition, a constant magnetic field strength was found for $n_{H_2} < 150$ cm$^{-3}$, which favors the scenario that gas accretion is guided by magnetic fields and increases the mass-to-flux ratio of clouds (Heitsch & Hartmann 2014).

In Section 2.4, our Bayesian analysis favors $B \propto n^{0.42}$ relation with a 95% confidence interval from 0.27 to 0.58, which is significantly lower than the index of 0.65 obtained in Crutcher et al. (2010). The lower power index suggests that the cloud collapse tends to follow the magnetic field instead of being isotropic, which is consistent with the scenario that magnetic fields are important in impeding the cloud collapse, predicted by the star formation models with strong magnetic fields (e.g Fiedler & Mouschovias 1993; Mouschovias & Morton 1991; Mocz et al. 2017).

The main difference between our analysis and Crutcher et al. (2010) is the sample selection. While our samples are selected from the IC5146 cloud, where the magnetic field is roughly uniform and the environment is similar, the samples used in Crutcher et al. (2010) were selected from 137 different clouds, where magnetic fields have random orientation and the environments could be different. Hence, the most straightforward explanation of the different results might be the diverse environments among molecular clouds.

Different $B$–$n$ power-law indices have been revealed in different clouds; an index of $0.41 \pm 0.04$ was found in NGC6334 (Li et al. 2015) and an index of $0.73 \pm 0.06$ was found in G028.23-00.19 (Hoq et al. 2017), which implies that the $B$–$n$ relation could be diverse among molecular clouds. Because the indices of 0.65 in Crutcher et al. (2010) was estimated using a uniform PDF of intrinsic magnetic field strength, their fitting is mainly determined by the upper boundary of the $B$–$n$ relation ($B_{max}$), and hence it is mainly determined by the clouds with the steepest $B$–$n$ relation among their samples, even if part of samples have flatter $B$–$n$ relation. Indeed, Figure 13 shows that nearly all of our samples are well below the $B_{max}$ boundary of the Crutcher et al. (2010) model. A uniform PDF $B$–$n$ model, by definition, indicates that the model has equal probabilities to match any $B < B_{max}$ values. Therefore, the Crutcher et al. (2010) model has the same probability to match our data as to match their data, and our data are actually consistent with that model. Nevertheless, even if our data are included in Crutcher et al. (2010)'s samples, the fitted $B_{max}$ is expected to be the same, because our data is not close to the upper boundary. This argument can also explain the consistency of the index of 0.47 derived in **?**, using a Gaussian PDF model, and the index of 0.66 derived in Crutcher et al. (2010), using a uniform PDF model, even though the former samples were included in the latter samples.

In addition to the diverse environments, the different power index could possibly be related to the target density regime or physical scale.

First, the power index might not be a constant over all density regimes. Our data set is limited in the local $n_{H_2} < 3 \times 10^3$ cm$^{-3}$ regime, while the Crutcher et al. (2010) data set represents the average slope over the $10^2 < n_{H_2} < 10^6$ cm$^{-3}$ regime. To extend the covered density region, we added a magnetic field estimation toward the dense hub-filament system embedded in the IC5146 cloud derived by Wang et al. (2019) in Figure 17. The estimated magnetic field strength is above the maximum magnetic field strength predicted by our fitted model by a factor of $\sim$3. Although we do not have samples to probe the $B$–$n$ relation in the $10^3 < n_{H_2} < 10^6$ cm$^{-3}$ regime, the high magnetic field strength estimated by Wang et al. (2019) might hint that the $B$–$n$ slope is probably steeper in the high density regime. Similarly, Li et al. (2015) fitted the OH samples ($5 \times 10^2 < n_{H_2} < 10^4$ cm$^{-3}$) and CN samples ($10^5 < n_{H_2} < 2 \times 10^6$ cm$^{-3}$) in Crutcher et al. (2010) separately, and found indices of $0.40 \pm 0.45$ and $0.04 \pm 0.67$, respectively.

Second, the numerical simulation of collapsing magnetized molecular clouds in Mocz et al. (2017) suggests that the $B$–$n$ relation may be scale dependent. On small scales ($< 10^4$ au), their simulation agreed with the previous models that power indices of 0.5 and 0.66 for the $B$–$n$ relation could be found in the strong and weak magnetic field cases, respectively; however, a power index of 0.5 was always found on large scales ($> 10^4$ au) in both the strong and weak magnetic field cases. Since the bin size we used to calculate magnetic field strength is 1.2 pc, the power index we obtained traces the large scale evolution. In contrast, the CN and OH Zeeman measurements used in Crutcher et al. (2010) may trace the evolution on smaller scales than ours, and hence reveal different $B$–$n$ relation. However, due to the wide range of distance among the Crutcher et al. (2010) samples, it is difficult to quantify which physical scale the observed index of 0.66 represents. More observations to reveal the $B$–$n$ relation at particular physical scale are still necessary to test this scenario.

## 4. SUMMARIES

1. With the new *Gaia* DR2 measurements, we found that the IC5146 cloud is likely consisted of two layers; the first layer, associated with the Cocoon Nebula, is at a distance of $\sim$ 800 pc, and the second layer, including the densest main filament, is at a distance of $\sim$ 600 pc.

2. The averaged H band polarization map shows an organized magnetic field pattern over the IC5146 cloud. The magnetic field is perpendicular to the main filament structure, but parallel to the filament extending to the north. The angular dispersion of the magnetic field is generally higher in the western part ($\sim 18°$) than in the eastern part ($\sim 12°$), possibly caused by the strong gravity or the multi-layers along the line of sight.

3. We estimated the magnetic field strength using the Davis-Chandrasekhar-Fermi method, and investigated how the magnetic field strength is scaled with the volume density. We used the Bayesian approach to fit the $B_{pos}$–$n$ relation assuming that the PDF of the intrinsic magnetic field is a truncated Gaussian or uniform distribution, and found that the uniform PDF can better explain the observed data. The derived power-law index ($\alpha$) is $\sim 0.4$, suggesting that magnetic field is important in regulating the collapse of the IC5146 cloud, which is consistent with the prediction of strong magnetic field models.

4. We estimated the mass-to-flux ratio using the $R_c$, $i$, and $H$ band data. The data in the optical bands tend to trace the magnetic field in the outer part of the cloud, while the infrared data trace the denser regions. The derived mass-to-flux ratio is generally subcritical in the outer part of the clouds but becomes transcritical or supercritical in the densest regions. The supercritical regions are consistent with the distribution of identified YSOs. This is consistent with the scenario that the cloud is generally supported by magnetic fields, but the gravity in the densest regions eventually overcome the magnetic field support and trigger star formation.

*Software:* Aplpy (Robitaille & Bressert 2012), Astropy (Astropy Collaboration et al. 2013), NumPy (Van Der Walt et al. 2011), PyMC3 (Salvatier et al. 2016), SciPy (Jones et al. 2001)

## REFERENCES

André, P., Men'shchikov, A., Bontemps, S., et al. 2010, A&A, 518, L102

Arzoumanian, D., André, P., Didelon, P., et al. 2011, A&A, 529, L6

Arzoumanian, D., André, P., Peretto, N., & Könyves, V. 2013, A&A, 553, A119

Astropy Collaboration, Robitaille, T. P., Tollerud, E. J., et al. 2013, A&A, 558, A33

Chandrasekhar, S., & Fermi, E. 1953 ApJ, 118, 113

Crutcher, R. M. 1999, ApJ, 520, 706

Crutcher, R. M., Nutter, D. J., Ward-Thompson, D., & Kirk, J. M. 2004, ApJ, 600, 279

Crutcher, R. M., Wandelt, B., Heiles, C., Falgarone, E., & Troland, T. H. 2010, ApJ, 725, 466

Crutcher, R. (2012) Ann. Rev. Astron. Astrophys., 50, 29-63

Davis, L., Jr., & Greenstein, J. L. 1951, ApJ, 114, 206

Dzib, S. A., Loinard, L., Ortiz-León, G. N., Rodríguez, L. F., & Galli, P. A. B. 2018, ApJ, 867, 151

Falceta-Gonçalves, D., Lazarian, A., & Kowal, G. 2008, ApJ, 679, 537

Fiedler, R. A., & Mouschovias, T. Ch. 1993, ApJ, 415, 680

Franco, G. A. P., Alves, F. O., & Girart, J. M. 2010, ApJ, 723, 146

Gaia Collaboration, Prusti, T., de Bruijne, J. H. J., et al. 2016, A&A, 595, A1

Gaia Collaboration, Brown, A. G. A., Vallenari, A., et al. 2018, A&A, 616, A1

Gómez, G. C., Vázquez-Semadeni, E., & Zamora-Avilés, M. 2018, MNRAS, 480, 2939

Harvey, P. M., Huard, T. L., Jørgensen, J. K., et al. 2008, ApJ, 680, 495-516

Heitsch, F., & Hartmann, L. 2014, MNRAS, 443, 230

Hoffman, M. D., & Gelman, A. 2011, The Journal of Machine Learning Research, 30.

Hoq, S., Clemens, D. P., Guzmán, A. E., & Cashman, L. R. 2017, ApJ, 836, 199

Inutsuka, S., Inoue, T., Iwasaki, K., & Hosokawa, T., 2015, A&A, 580, A49

Jones, E., Oliphant, E., Peterson, P., et al. 2001, http://www.scipy.org/

Kim, E.-j., & Diamond, P. H. 2002, ApJL, 578, L113

Lada, C. J., Alves, J., & Lada, E. A. 1999, ApJ, 512, 250

Lazarian, A., Esquivel, A., & Crutcher, R. 2012, ApJ, 757, 154

Li, H.-b., Fang, M., Henning, T., & Kainulainen, J. 2013, MNRAS, 436, 3707

Li, H.-b., Yuen, K.-H, Otto, F., et al. 2015, Nature, 520, 518

Li, P. S., McKee, C. F., & Klein, R. I. 2015, MNRAS, 452, 2500

Mac Low, M.-M., & Klessen, R. S. 2004, Rev. Mod. Phy., 76, 125

McKee, C. F., & Ostriker, E. C. 2007, ARA&A, 45, 565

Men'shchikov, A., André, P., Didelon, P., et al. 2010, A&A, 518, L103

Miville-Deschênes, M., Martin, P. G., Abergel, A., et al. 2010, A&A, 518, L104

Molinari, S., Swinyard, B., Bally, J., et al. 2010, A&A, 518, L100

Mouschovias, T. C., & Morton, S. A. 1991, ApJ, 371, 296

Mocz, P., Burkhart, B., Hernquist, L., McKee, C. F., & Springel, V. 2017, ApJ, 838, 40

Nakamura, F., & Li, Z. 2008, ApJ, 687, 354

Nakano, T., & Nakamura, T. 1978, PASJ, 30, 671

Ostriker, E. C., Stone, J. M., & Gammie, C. F. 2001, ApJ, 546, 980

Padoan, P., & Nordlund, A. 2002, ApJ, 576, 870

Palmeirim, P., André, P., Kirk, J., et al. 2013, A&A, 550, A38

Pillai, T., Kauffmann, J., Tan, J. C., et al. 2015, ApJ, 799, 74

Planck Collaboration, Ade, P. A. R., Aghanim, N., et al. 2016, A&A, 586, A138

Price, D. J., & Bate, M. R. 2008, MNRAS, 385, 1820

Robitaille, T., & Bressert, E. 2012, Astrophysics Source Code Library, ascl:1208.017

Salvatier J, Wiecki TV, Fonnesbeck C. 2016, Probabilistic programming in Python using PyMC3. PeerJ Computer Science 2:e55 https://doi.org/10.7717/peerj-cs.55

Santos-Lima, R., Lazarian, A., de Gouveia Dal Pino, E. M., & Cho, J. 2010, ApJ, 714, 442

Seifried, D., & Walch, S. 2015, MNRAS, 452, 2410

Shimajiri, Y., André, P., Palmeirim, P., et al. 2019, A&A, 623, A16

Sugitani, K., Nakamura, F., Watanabe, M., et al. 2011, ApJ, 734, 63

Van Der Walt, S., Colbert, S. C., & Varoquaux, G. 2011, "The NumPy array: A structure for efficient numerical computation" Comput. Sci. Eng. 13(2), 22-30

Van Loo, S., Keto, E., & Zhang, Q. 2014, ApJ, 789, 37

Vehtari, A., Gelman, A., Gabry, J.. 2017, Statistics and Computing, 27, 5, 1413. https://doi.org/10.1007/s11222-016-9696-4

Wang, J.-W., Lai, S.-P., Eswaraiah, C., et al. 2017, ApJ, 849, 157

Wang, J.-W., Lai, S.-P., Eswaraiah, C., et al. 2019, ApJ, 876, 42

Ward-Thompson, D., Kirk, J. M., André, P., et al. 2010, A&A, 518, L92